FOR UNRESTRICTED DISTRIBUTION
DATE 10/18/90 WEC

FOR UNRESTRICTED DISTRIBUTION
DATE 10/18/90 WEC

Westinghouse Energy Systems

9102130194 910206
PDR ADOCK 05000395
P PDR

WCAP 12593 SG-90-05-045

V. C. SUMMER
EVALUATION FOR TUBE VIBRATION INDUCED FATIGUE

OCTOBER 1990

APPROVED: for M. J. WOOTTEN, MANAGER
STEAM GENERATOR TECHNOLOGY AND ENGINEERING

This document contains information proprietary to Westinghouse Electric Corporation. It is submitted in confidence and is to be used solely for the purpose for which it is furnished and is to be returned upon request. This document and such information is not to be reproduced, transmitted, disclosed or used otherwise in whole or in part without written authorization of Westinghouse Electric Corporation, Energy Systems Business Unit.

WESTINGHOUSE ELECTRIC CORPORATION
NUCLEAR SERVICE DIVISION
P.O. BOX 355
PITTSBURGH, PENNSYLVANIA 15230

©1990 Westinghouse Electric Corporation

FOREWORD

This nonproprietary report bears a Westinghouse copyright notice. The NRC is permitted to make the number of copies of this report necessary for its internal use and such additional copies which are necessary in order to have one copy available for public viewing in the appropriate docket files in the public document room in Washington, D.C. and in local public document rooms as may be required by NRC regulations if the number of copies submitted is insufficient for this purpose. The NRC is not authorized to make copies for the personal use of members of the public who make use of the NRC public document rooms. Copies of this report on portions thereof made by the NRC must include the copyright notice.

ABSTRACT

On July 15, 1987, a steam generator tube rupture event occurred at the North Anna Unit 1 plant. The cause of the tube rupture has been determined to be high cycle fatigue. The source of the loads associated with the fatigue mechanism is a combination of a mean stress level in the tube with a superimposed alternating stress. The mean stress is the result of applied loading, manufacturing-induced residual stress and denting of the tube at the top tube support plate, while the alternating stress is due to out-of-plane deflection of the tube U-bend attributed to flow induced vibration. For tubes without AVB support, local flow peaking effects are a significant contributor to tube vibration amplitudes.

This report documents the evaluation of steam generator tubing at V. C. Summer for susceptibility to fatigue-induced cracking of the type experienced at North Anna Unit 1. The evaluation utilizes operating conditions specific to V. C. Summer to account for the plant specific nature of the tube loading and response. The evaluation also includes reviews of eddy current data for V. C. Summer to establish AVB locations. This report provides background of the event which occurred at North Anna, a criteria for fatigue assessment, a summary of test data which support the analytical approach, field measurement results showing AVB positions, thermal hydraulic analysis results, and calculations to determine tube mean stress, stability ratio, tube stress ratio, and accumulated fatigue usage. This evaluation concludes that seven tubes were potentially susceptible to fatigue, and required ameliorative action.

Such action was completed in April, 1990, with the installation of a cable damper, a hot leg solid plug, and a cold leg sentinel plug, in each of the seven aforementioned tubes. No further ameliorative action is required, and the tubes remaining in service in the V. C. Summer steam generators are not expected to be susceptible to high-cycle fatigue rupture at the top tube support plate in a manner similar to the rupture which occurred at North Anna Unit #1 assuming operation of the plant through the end of the operating license at a full power steam pressure above 905 psia.

SUMMARY OF ABBREVIATIONS

ASME	-	American Society of Mechanical Engineers
ATHOS	-	Analysis of the Thermal Hydraulics of Steam Generators
AVB	-	Anti-Vibration Bar
AVT	-	All Volatile Treatment
ECT	-	Eddy Current Test
EPRI	-	Electric Power Research Institute
FFT	-	Fast Fourier Transform
FLOVIB	-	Flow Induced Vibrations
MEVF	-	Modal Effective Void Fraction
OD	-	Outside Diameter
RMS	-	Root Mean Square
SR	-	Stability Ratio
TSP	-	Tube Support Plate
°F	-	degrees Fahrenheit
hr	-	hour
ksi	-	measure of stress - 1000 pounds per square inch
lb	-	pound
mils	-	0.001 inch
MW	-	megawatt
psi	-	measure of stress - pounds per square inch
psia	-	measure of pressure - absolute

TABLE OF CONTENTS

SECTION

TABLE OF CONTENTS (CONTINUED)

SECTION

LIST OF FIGURES

FIGURE

FIGURE

FIGURE

LIST OF FIGURES (Continued)

FIGURE

LIST OF FIGURES (Continued)

LIST OF TABLES

TABLE

TABLE

1.0 INTRODUCTION

This report documents the evaluation of steam generator tubing at V. C. Summer for susceptibility to fatigue-induced cracking of the type experienced at North Anna Unit 1 in July, 1987. The evaluation includes three-dimensional flow analysis of the tube bundle, air tests performed to support the vibration analytical procedure, field measurements to establish AVB locations, structural and vibration analysis of selected tubes, and fatigue usage calculations to predict cumulative usage for critical tubes. The evaluation utilizes operating conditions specific to V. C. Summer in order to account for plant specific features of the tube loading and response.

Section 2 of the report provides a summary of the V. C. Summer evaluation results and overall conclusions. Section 3 provides background of the tube rupture event which occurred at North Anna Unit 1 including results of the examination of the ruptured tube and a discussion of the rupture mechanism. The criteria for predicting the fatigue usage for tubes having an environment conducive to this type of rupture are discussed in Section 4. Section 5 provides a summary of test data which supports the analytical vibration evaluation of the candidate tubes. A summary of field measurements used to determine AVB locations and to identify unsupported tubes is provided in Section 6. Section 7 provides the results of a thermal/hydraulic analysis to establish flow field characteristics at the top support plate which are subsequently used to assist in identifying tubes which may be dynamically unstable. Section 8 presents an update of the methodology originally used to evaluate the tube rupture at North Anna Unit 1. The final section, Section 9, presents results of the structural and vibration assessment. This section describes tube mean stress, stability ratio and stress ratio distributions, and accumulated fatigue usage for the V. C. Summer steam generator small radius U-tubes.

2.0 SUMMARY AND CONCLUSIONS

The V. C. Summer steam generators have been evaluated for the susceptibility to a fatigue rupture of the type experienced at Row 9 Column 51 (R9C51) of Steam Generator C at North Anna Unit 1. The evaluation used Eddy Current Test (ECT) data supplied by SCE&G and interpreted by Westinghouse.

2.1 Background

The initiation of the circumferential crack in the tube at the top of the top tube support plate at North Anna 1 has been attributed to limited displacement, fluidelastic instability. This condition is believed to have prevailed in the R9C51 tube since the tube experienced denting at the support plate. A combination of conditions were present that led to the rupture. The tube was not supported by an anti-vibration bar (AVB), had a higher flow field due to local flow peaking as a result of non-uniform insertion depths of AVBs, had reduced damping due to denting at the top support plate, and had reduced fatigue properties due to the environment of the all volatile treatment (AVT) chemistry of the secondary water and the additional mean stress from the denting.

2.2 Evaluation Criteria

The criteria established to provide a fatigue usage less than 1.0 for a finite period of time (i.e., 40 years) is a 10% reduction in stability ratio that provides at least a 58% reduction in stress amplitude (to < 4.0 ksi) for a Row 9 tube in the North Anna 1 steam generators (SG's). This reduction is required to produce a fatigue usage of < 0.021 per year for a Row 9 tube in North Anna and therefore greater than 40 year fatigue design basis. This same fatigue criteria is applied as the principal criteria in the evaluation of V. C. Summer tubing.

The fluidelastic stability ratio is the ratio of the effective velocity divided by the critical velocity. A value greater than unity (1.0) indicates instability. The stress ratio is the expected stress amplitude in a

V. C. Summer tube divided by the stress amplitude for the North Anna 1, R9C51 tube.

Displacements are computed for unsupported U-bend tubes in Rows 13 and inward, (descending row number) using relative stability ratios to R9C51 of North Anna 1 and an appropriate power law relationship based on instability displacement versus flow velocity. Different U-bend radius tubes and tube sizes have different stiffness and frequency and, therefore, different stress and fatigue usage per year than the Row 9 North Anna tube. These effects are accounted for in a stress ratio technique. The stress ratio is formulated so that a stress ratio of 1.0 or less produces acceptable stress amplitudes and fatigue usage for the V. C. Summer tubing assuming that the tubing remains in service for the balance of the plant operating license at the operating conditions for the reference fuel cycle analyzed. Therefore, a stress ratio less than 1.0 provides the next level of acceptance criteria for unsupported tubes for which the relative stability ratio, including flow peaking, exceed 0.9.

The stability ratios for V. C. Summer tubing, the corresponding stress and amplitude, and the resulting cumulative fatigue usage must be evaluated relative to the ruptured tube at Row 9 Column 51, North Anna 1, Steam Generator C, for two reasons. The local effect on the flow field due to AVB insertion depths is not calculable with available analysis techniques and is determined by test as a ratio between two AVB configurations. In addition, an analysis and examination of the ruptured tube at North Anna 1 provided a range of initiating stress amplitudes, but could only bound the possible stability ratios that correspond to these stress amplitudes. Therefore, to minimize the influence of uncertainties, the evaluation of V. C. Summer tubing has been based on relative stability ratios, relative flow peaking factors, and relative stress ratios.

The criteria for establishing that a tube has support from an AVB, is that it must have at least one-sided AVB support present at the tube centerline. The criteria is based on test results which show that one-sided AVB support is sufficient to limit the vibration amplitude for fluidelastic excitation. AVB support is established by analysis of eddy current (EC) measurements and is a key factor in determining the local flow peaking factors. The local flow peaking produces increased local velocities which cause an increase in stability ratio. A small change in the stability ratio causes a significant change in stress amplitude. The relative flow peaking factors of V. C. Summer tubing without direct AVB support have been determined by test. These flow peaking factors, normalized to the North Anna R9C51 peaking, are applied to relative stability ratios determined by 3-D tube bundle flow analysis, to obtain the combined relative stability ratio used in the stress ratio determination.

2.3 Denting Evaluation

The Eddy Current (EC) tapes were evaluated [

]^{a,c} to determine the condition of the tube/top tube support interface of the unsupported tubes having potential flow peaking. Because of the significance of the top tube support plate crevice conditions on the analysis and the potential for further corrosion at the top tube support plate since the October 1988 EC inspection, the EC analysis assumed that top tube support plate crevices were dented (i.e. having "corrosion with magnetite" or "tube denting with deformation") unless they could conclusively be demonstrated to be otherwise. Analyses of eddy current (EC) data for V. C. Summer shows the presence of "corrosion with magnetite" in roughly half of the tube/TSP crevices. Of the twenty-five (25) tube eddy current results from the October, 1988, inspection that were evaluated for top tube support plate corrosion, eleven (11) were found to be magnetite-packed at one or both top tube support plate legs, none showed denting with deformation, and the remaining fourteen (14) showed no detectable magnetite or corrosion. For conservatism in the evaluation, all of the tubes evaluated are postulated to be dented. The effect of denting on the fatigue usage of the tube has been conservatively maximized by assuming the maximum effect of mean stress in the tube fatigue usage evaluation and by incorporating reduced damping in the tube vibration evaluation.

2.4 AVB Insertion Depths

The V. C. Summer SGs have two sets of Alloy 600 AVBs. The 'inner' or lower AVBs have a rectangular cross-section and extend into the tube bundle approximately as far as Row 10. They provide a nominal total clearance between a tube without ovality and the surrounding AVBs of [$]^{a,c}$ inch.

The outer (or upper) AVBs also have a rectangular cross section, and extend into the tube bundle approximately as far as Row 21, providing a nominal tube-to-AVB clearance comparable to the inner AVBs. Since the purpose of this analysis is to evaluate the potentially unsupported tubes at or near the point of maximum AVB insertion, only the dimensions and EC data pertaining to the inner AVBs are required.

The eddy current data were analyzed by Westinghouse to identify the number of tube/AVB intersections and the location of these intersections relative to the apex of a given tube. This information was used in calculations to determine the deepest penetration of a given AVB into the tube bundle. For the area of interest in the V. C. Summer steam generators, the AVB support of the tube can normally be verified if EC data shows both legs of the lower AVB, one on each side (hot leg - cold leg) of the U-bend. This is the preferred method of establishing tube support.

If only the apex of a V. C. Summer AVB assembly is near or touching the apex of a tube U-bend, only one AVB signal may be seen. In this case, adequate tube support cannot be assumed without supplemental input. Support can be determined if 'projection' calculations based on AVB intercepts of higher row number tubes in the same and adjacent columns verify insertion depth to a point below the tube centerline. Maps of the AVB insertion depths for V. C. Summer are shown in Figures 6-2 thru 6-4. The AVB maps list the results of the 'projection' calculations from the smallest row tube for which suitable data exist to make a projection.

At tube locations where flow peaking effects could be significant, determination of only tube support conditions may not be sufficient to adequately define flow peaking factors. Flow peaking factor can, in some cases, [

]^{a,c}

2.5 Flow Peaking Factors

Tests were performed modeling V. C. Summer tube and AVB geometries to determine the flow peaking factors for various AVB configurations relative to the North Anna R9C51 peaking factor. The test results were used to define an upper bound of the ratio relative to the R9C51 configuration.

2.6 Tube Vibration Evaluation

The calculation of relative stability ratios for V. C. Summer makes use of detailed tube bundle flow field information computed by the ATHOS steam generator thermal/hydraulic analysis code. Code output includes three-dimensional distributions of secondary side velocity, density, and void fraction, along with primary fluid and tube wall temperatures. Distributions of these parameters have been generated for every tube of interest in the V. C. Summer tube bundles based on recent full power operating conditions. This information was factored into the tube vibration analysis leading to the relative stability ratios.

Relative stability ratios of V. C. Summer (Row 8 through Row 12) tubing versus R9C51 of North Anna 1 are plotted in Figure 9-5. These relative stability ratios include relative flow peaking factors. The stress ratios for V. C. Summer are given in Figure 9-6 for tubes in the dented condition. These also include the relative flow peaking effect, and are calculated based on clamped tube conditions with denting (with deformation) at the top tube support plate.

Fatigue usages were calculated for current operating conditions and for the full power steam pressures calculated for plugging levels of 12% and 15%. Four tubes, SG-A R9C83, SG-B R9C56, SG-C R12C5 and SG-C R13C5, if previously dented or if becoming dented at the beginning of an operating cycle with current operating conditions, such that the tube becomes rigidly clamped within the top tube support, could potentially have tube fatigue usage factors exceeding 1.0 within the cycle, and therefore require ameliorative action. With the exception of SG-B R9C56, which was evaluated as having magnetite packing at one of the two top tube support plate intersections, all of these four tubes were evaluated from the October 1988 outage inspection data as "clean" at the top tube support plate intersections. Two additional tubes, SG-C R9C29 (magnetite in one top TSP and clean in the other) and SG-C R10C23 (magnetite in both top TSP crevices), potentially have current accumulated fatigue usages as high as 1.0, if it is conservatively assumed that denting began at the start of the first fuel cycle, and also therefore require ameliorative action. SG-C R9C106 was evaluated as having no denting at the top tube support plate elevation in the October 1988 EC inspection, but may have accumulated as much as 0.34 fatigue usage if it became dented or magnetite-packed at the beginning of the subsequent cycle. If dented and operating at Cycle 5 conditions, it could continue to accumulate fatigue usage at the rate of 0.34 per year, and was recommended for preventive action. Utilizing the past operating history and Cycle 5 operating conditions (941 psia steam pressure), the evaluation found that all other tubes are acceptable for continued operation through the end of the plant operating license.

To assist SCE&G in evaluating operational issues associated with cable damper modification options, the lowest added damping value determined from available tests was assumed to be provided by cable dampers in the seven tubes of interest for V. C. Summer. With this assumed minimum added damping value of [ ],^{a,c} all of the stress ratios in the seven tubes of interest are below [ ],^{a,c} with the highest being SG-C R13C5, having a stress ratio of [ ]^{a,c}. R12C5 would have a stress ratio of [ ]^{a,c}, and the remaining five tubes under consideration would have stress ratios of [ ]^{a,c} or less. With this assumption, tubes that had not initiated a crack would be acceptable for continued operation with a cable damper installed.

Based upon a review of the operational, maintenance, and modification installation factors associated with the modification options, SCE&G decided to install cable dampers into the seven tubes listed above. Since [

]^{a,c}

A summary listing of the unsupported critical tubes and pertinent vibration parameters (prior to installation of cable dampers) is given in Table 9-2.

An additional fatigue evaluation of the V. C. Summer tubing was performed to examine the effect of reduced steam pressure and coastdown power levels, with the objective of demonstrating the acceptability of the tube remaining in service with the highest stress ratio that does not exceed the 1.0 stress ratio criterion. Parametric analysis was performed to determine the relative stability ratio (RSR) multipliers and stress ratios for full power steam pressures below the reference steam pressure (941 psia) and it was determined that the limiting tube, SG-A R9C55, does not exceed the 1.0 stress ratio criterion for steam pressures above 905 psia. Since SCE&G is considering power coastdown operation, the RSR multipliers were also evaluated assuming a constant volumetric steam flow for pressures below 905 psia. (The 905 psia steam pressure is a lower bound, full power steam pressure value; V. C. Summer turbine tests indicate the "best estimate" value of the Valves Wide Open (VWO) steam pressure to be 915 psia). For the reduced power levels associated with operation below the assumed 905 psia VWO limit, the RSR multipliers decrease, and the fatigue results remain bounded. Therefore, assuming that the worst case tube (SG-A R9C55) has been dented since the first cycle and the turbine Valves Wide Open limit is not reduced below 905 psia, all tubes remaining in service at V. C. Summer are acceptable for operation through the end of the current operating license with power levels at or below 2785 MWt.

2.7 Overall Conclusion

Seven tubes were recommended for preventive action: SG-A R9C83, SG-B R9C56, SG-C R12C5, SG-C R13C5, SG-C R10C23, SG-C R9C29, and SG-C R9C106. These tubes were removed from service in April 1990 with the installation of cable dampers, hot leg plugs, and cold leg sentinel plugs. The tubes remaining in service in the V. C. Summer steam generators are not expected to be susceptible to high-cycle fatigue rupture at the top tube support plate in a manner similar to the rupture which occurred at North Anna #1, assuming that the turbine Valves Wide Open limit is not reduced below 905 psia, through the end of the current operating license with power levels at or below 2785 MWt.

3.0 BACKGROUND

On July 15, 1987, a steam generator tube rupture occurred at the North Anna Unit 1. The ruptured tube was determined to be Row 9 Column 51 in steam generator "C". The location of the opening was found to be at the top tube support plate on the cold leg side of the tube and was circumferential in orientation with a 360 degree extent.

3.1 North Anna Unit 1 Tube Rupture Event

The cause of the tube rupture has been determined to be high cycle fatigue. The source of the loads associated with the fatigue mechanism has been determined to be a combination of a mean stress level in the tube and a superimposed alternating stress. The mean stress has been determined to have been increased to a maximum level as the result of denting of the tube at the top tube support plate and the alternating stress has been determined to be due to out-of-plane deflection of the tube U-bend above the top tube support caused by flow induced vibration. These loads are consistent with a lower bound fatigue curve for the tube material in an AVT water chemistry environment. The vibration mechanism has been determined to be fluid elastic, based on the magnitude of the alternating stress.

A significant contributor to the occurrence of excessive vibration is the reduction in damping at the tube-to-tube support plate interface caused by the denting. Also, the absence of antivibration bar (AVB) support has been concluded to be required for vibration to occur. The presence of an AVB support restricts tube motion and thus precludes the deflection amplitude required for fatigue. Inspection data show that an AVB is not present for the Row 9 Column 51 tube but that the actual AVB installation depth exceeded the minimum requirements in all cases with data for AVBs at many other Row 9 tubes. Also contributing significantly to the level of vibration, and thus loading, is the local flow field associated with the detailed geometry of the steam generator, i.e., AVB insertion depths. In addition, the fatigue properties of the tube reflect the lower range of properties expected for an AVT environment. In summary, the prerequisite conditions derived from the evaluations were concluded to be:

Fatigue Requirements	Prerequisite Conditions
Alternating stress	Tube vibration - Dented support - Flow excitation - Absence of AVB
Mean stress	Denting in addition to applied stress
Material fatigue properties	AVT environment - Lower range of properties

3.2 Tube Examination Results

Fatigue was found to have initiated on the cold leg outside surface of tube R9C51 immediately above the top tube support plate. No indication of significant accompanying intergranular corrosion was observed on the fracture face or on the immediately adjacent OD surfaces. Multiple fatigue initiation sites were found with major sites located at 110°, 120°, 135° and 150°, Figure 3-1. The plane of the U-bend is located at 45° with the orientation system used, or approximately 90° from the geometric center of the initiation zone at Section D-D. High cycle fatigue striation spacings approached 1 micro-inch near the origin sites, Figure 3-2. The early crack front is believed to have broken through-wall from approximately 100° to 140°. From this point on, crack growth is believed (as determined by striation spacing, striation direction, and later observations of parabolic dimples followed by equiaxed dimples) to have accelerated and to have changed direction with the resulting crack front running perpendicular to the circumferential direction.

3.3 Mechanism Assessment

To address a fatigue mechanism and to identify the cause of the loading, any loading condition that would cause cyclic stress or steady mean stress had to be considered. The analysis of Normal, Upset and Test conditions indicated a relatively low total number of cycles involved and a corresponding low fatigue usage, even when accounting for the dented tube condition at the plate. This analysis also showed an axial tensile stress contribution at the tube OD a short distance above the plate from operating pressure and temperature, thus providing a contribution to mean stress. Combining these effects with denting deflection on the tube demonstrated a high mean stress at the failure location. Vibration analysis for the tube developed the characteristics of first mode, cantilever response of the dented tube to flow induced vibration for the uncracked tube and for the tube with an increasing crack angle, beginning at 90° to the plane of the tube and progressing around on both sides to complete separation of the tube.

Crack propagation analysis matched cyclic deformation with the stress intensities and striation spacings indicated by the fracture inspection and analysis. Leakage data and crack opening analysis provided the relationship between leak rate and circumferential crack length. Leakage versus time was then predicted from the crack growth analysis and the leakage analysis with initial stress amplitudes of 5, 7, and 9 ksi. The comparison to the estimate of plant leakage (performed after the event) showed good agreement, Figure 3-3.

Based on these results, it followed that the predominant loading mechanism responsible is a flow-induced, tube vibration loading mechanism. It was shown that of the two possible flow-induced vibration mechanisms, turbulence and fluidelastic instability, that fluidelastic instability was the most probable cause. Due to the range of expected initiation stress amplitudes (4 to 10 ksi), the fluidelastic instability would be limited in displacement to a range of approximately [ ]^{a,c}. This is less than the distance between tubes at the apex, [ ]^{a,c}. It was further confirmed that displacement prior to the rupture was limited since no indication of tube U-bend (apex region) damage was evident in the eddy-current signals of adjacent tubes.

Given the likelihood of limited displacement, fluidelastic instability, a means of establishing the change in displacement, and corresponding change in stress amplitude, was developed for a given reduction in stability ratio (SR). Since the rupture was a fatigue mechanism, the change in stress amplitude resulting from a reduction in stability ratio was converted to a fatigue usage benefit through the use of the fatigue curve developed. Mean stress effects were included due to the presence of denting and applied loadings. The results indicated that a 10% reduction in stability ratio is needed (considering the range of possible initiation stress amplitudes) to reduce the fatigue usage per year to less than 0.02 for a tube similar to Row 9 Column 51 at North Anna Unit 1.

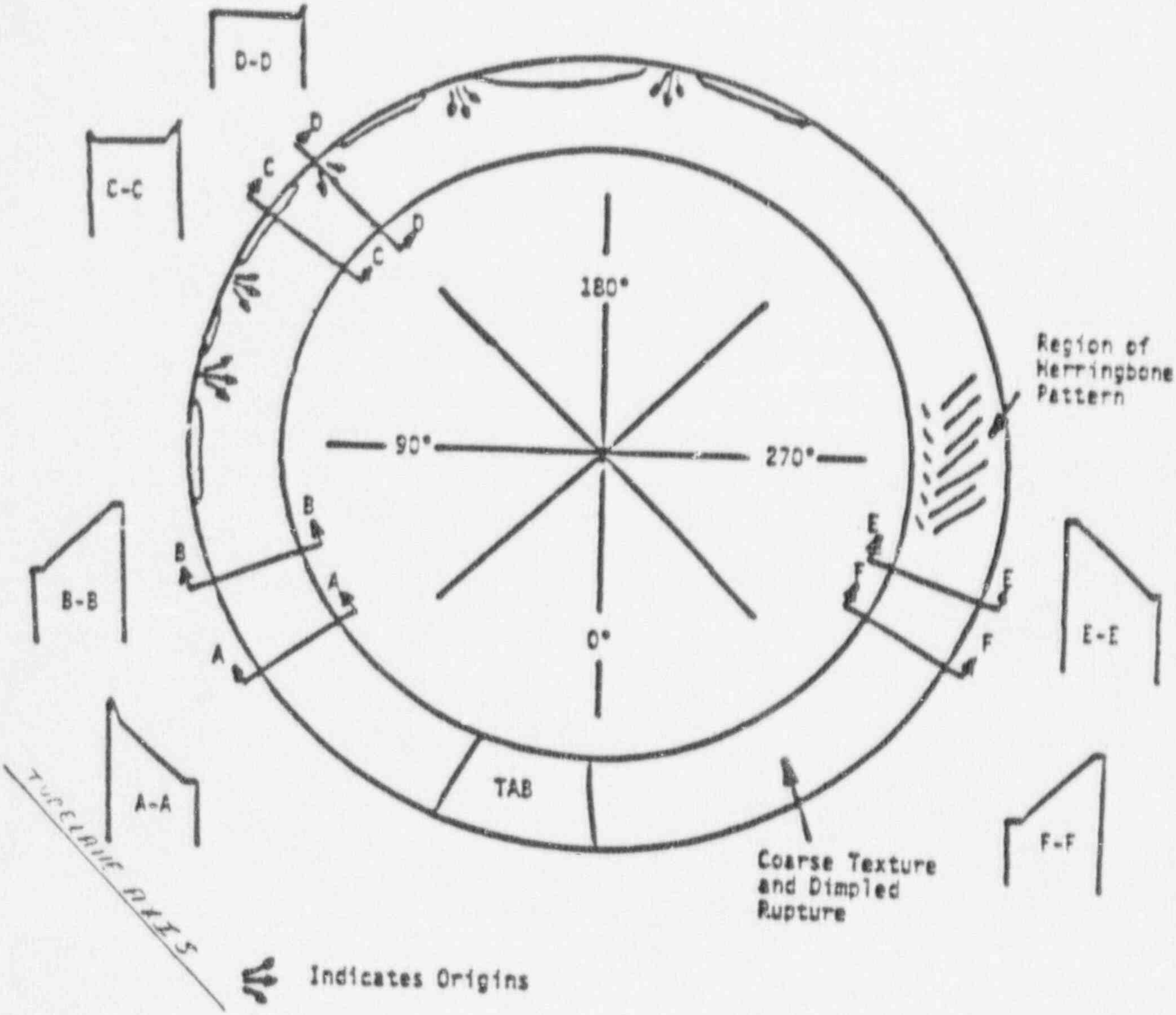

Figure 3-1 Approximate Mapping of Fracture Surface of Tube R9C51, S/G "C" Cold Leg, North Anna Unit 1

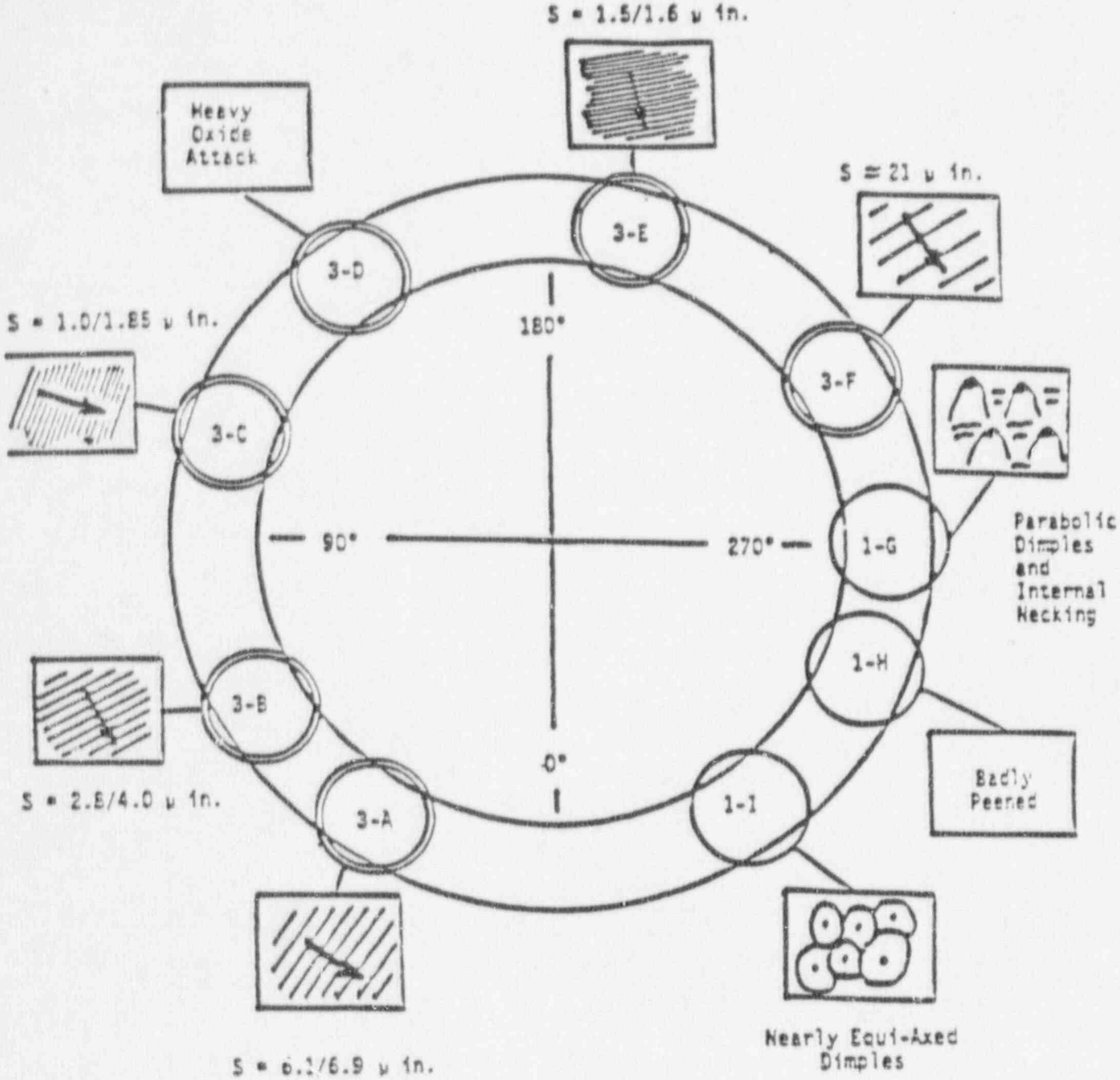

Note: Arrows Indicate Direction of Fracture Propagation

Figure 3-2 Schematic Representation of Features Observed During TEM Fractographic Examination of Fracture Surface of Tube R9C51, S/G "C" Cold Leg, North Anna Unit 1

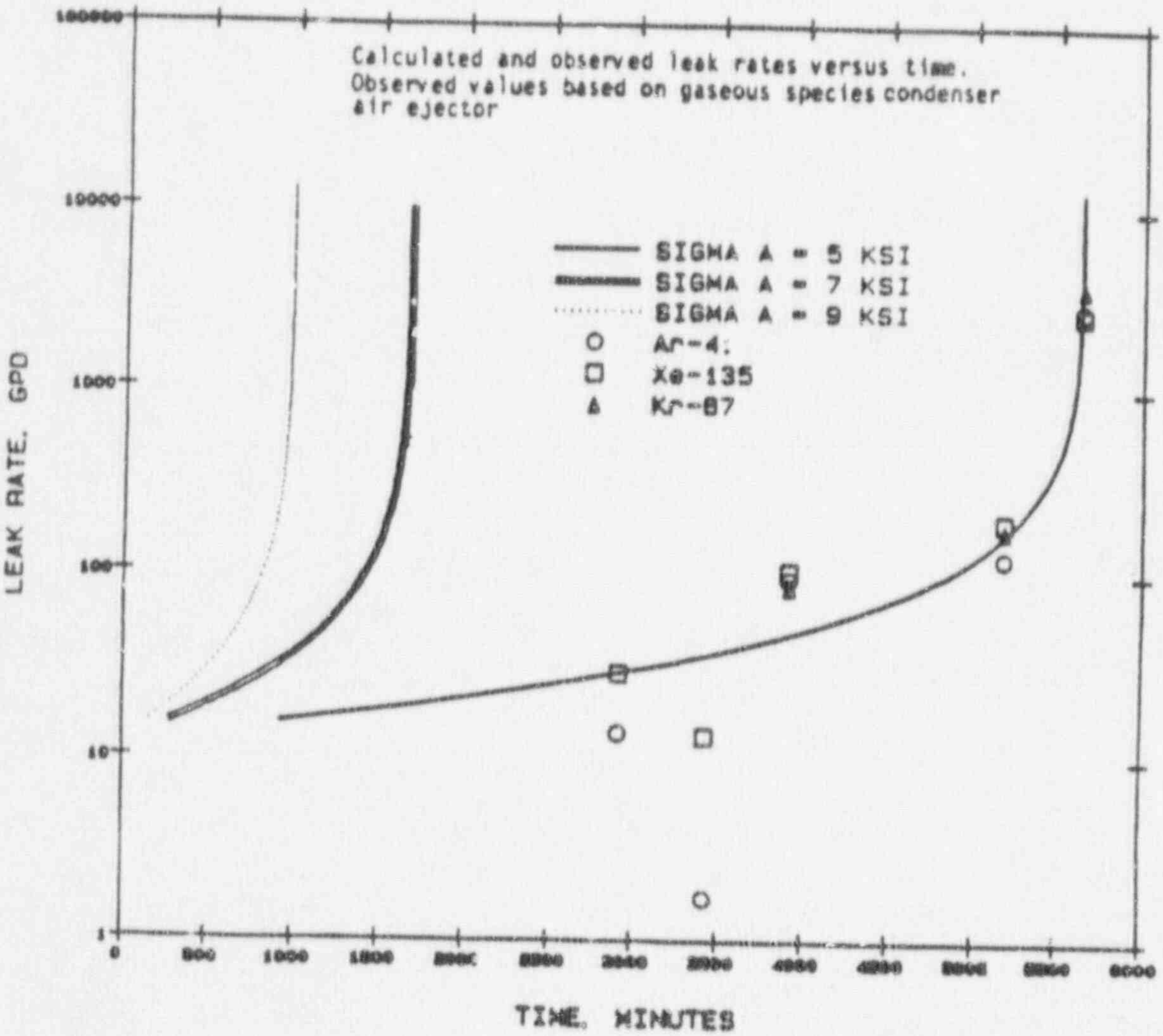

Figure 3-3 Calculated and Observed Leak Rates Versus Time

4.0 CRITERIA FOR FATIGUE ASSESSMENT

The evaluation method and acceptance criteria are based on a relative comparison with the Row 9 Column 51 tube of Steam Generator C, North Anna Unit 1. This approach is necessary because (1) methods for direct analytical prediction of actual stability ratios incorporate greater uncertainties than a relative ratio method, and (2) the stress amplitude (or displacement) associated with a specific value of stability ratio can only be estimated by the analysis of North Anna Unit 1. For these reasons, the North Anna Unit 1 tubing evaluation was done on a relative basis to Row 9 Column 51 and a 10% reduction in stability ratio criteria was established to demonstrate that tubes left in service would be expected to have sufficiently low vibration stress to preclude future fatigue rupture events.

To accomplish the necessary relative assessment of V. C. Summer tubing to Row 9 Column 51 of North Anna Unit 1, several criteria are utilized. First, stability ratios are calculated for V. C. Summer tubes based on flow fields predicted by 3-D thermal hydraulic models and ratioed to the stability ratio for Row 9 Column 51 at North Anna Unit 1 based on a flow field obtained with a 3-D thermal hydraulic model with the same degree of refinement. These ratios of stability ratio (called relative stability ratios) for each potentially unsupported U-bend in the V. C. Summer steam generators should be equivalent to $\leq$ 0.9 of R9C51, North Anna 1 (meeting the 10% reduction in stability ratio criteria). This provides the first level of screening of susceptible tubes incorporating all tube geometry and flow field differences in the tube dynamic evaluation. It has the inherent assumption, however, that each tube has the same local, high flow condition present at Row 9 Column 51, North Anna Unit 1. To account for these differences, flow peaking factors can be incorporated in the relative stability ratios and the stress ratios.

The next step is to obtain stress ratios, the ratio of stress in the V. C. Summer tube of interest to the stress in Row 9 Column 51, North Anna Unit 1, and after incorporating the requirement that the relative stability ratio to Row 9 Column 51 (R9C51) for the tube of interest is equivalent to $\leq$ 0.9, require the stress ratio to be $\leq$1.0. The stress ratio incorporates the tube geometry differences with R9C51 in relation to the stress calculation and also incorporates the ratio of flow peaking factor for the tube of interest to the flow peaking factor for R9C51 (flow peaking factor is defined in Section 4.2). This should provide that all tubes meeting this criteria have stress amplitudes equivalent to $\leq$ 4.0 ksi.

Finally, the cumulative fatigue usage for plant operation to date and for continued operation with the same operating parameters is evaluated. A fatigue usage $\leq$ 1.0 may not be satisfied by meeting the stress ratio criteria using the reference operating cycle evaluation since the reference cycle does not necessarily represent the exact duty cycle to date. Therefore, the time history of operation is evaluated on a normalized basis and used together with the stress ratio to obtain a stress amplitude history. This permits the calculation of current and future fatigue usage for comparison to 1.0.

4.1 Stability Ratio Reduction Criteria

For fluidelastic evaluation, stability ratios are determined for specific configurations of a tube. These stability ratios represent a measure of the potential for flow-induced tube vibration during service. Values greater than unity (1.0) indicate instability (see Section 5.1).

Motions developed by a tube in the fluidelastically unstable mode are quite large in comparison to the other known mechanisms. The maximum modal displacement (at the apex of the tube) is linearly related to the bending stress in the tube just above the cold leg top tube support plate. This relationship applies to any vibration in that mode. Thus, it is possible for an unstable, fixed boundary condition tube to deflect an amount in the U-bend which will produce fatigue inducing stresses.

The major features of the fluidelastic mechanism are illustrated in Figure 4-1. This figure shows the displacement response (LOG D) of a tube as a function of stability ratio (LOG SR). A straight-line plot displayed on log-log coordinates implies a relation of the form $y = A(x)^n$, where A is a constant, x is the independent variable, n is the exponent (or power to which x is raised), and y is the dependent variable. Taking logs of both sides of this equation leads to the slope-intercept form of a straight-line equation in log form, $\log y = c + n \log x$, where $c = \log A$ and represents the intercept and n is the slope. In our case the independent variable x is the stability ratio SR, and the dependent variable y is tube (fluidelastic instability induced) displacement response D, and the slope n is renamed s.

From experimental results, it is known that the turbulence response curve (on log-log coordinates) has a slope of approximately [ ]^{a,b,c}. Test results also show that the slope for the fluidelastic response depends somewhat on the instability displacement (response amplitude). It has been shown by tests that a slope of [ ]^{a,b,c} is a range of values corresponding to displacement amplitudes in the range of [ ]^{a,c}, whereas below [ ]^{a,c} are conservative values.

The reduction in response obtained from a stability ratio reduction can be expressed by the following equation:

[ ]^{a,c}

where D_1 and SR_1 are the known values at the point corresponding to point 1 of Figure 4-1 and D_2 and SR_2 are values corresponding to any point lower on this curve. Therefore, this equation can be used to determine the reduction in displacement response for any given reduction in stability ratio.

This equation shows that there is benefit derived from even a very small percentage change in the stability ratio. It is this reduction in displacement for a quite small reduction in stability ratio that formed the basis for demonstrating that a 10% reduction in stability ratio would be sufficient to prevent Row 9 Column 51 from rupturing by fatigue.

The fatigue curve developed for the North Anna Unit 1 tube at R9C51 is from [

]a,c. Thus,

[ ]a,c

where, σ_a' is the equivalent stress amplitude to σ_a that accounts for a maximum stress of σ_y, the yield strength. The -3 sigma curve with mean stress effects is shown in Figure 4-2 and is compared to the ASME Code Design Fatigue Curve for Inconel 600 with the maximum effect of mean stress. The curve utilized in this evaluation is clearly well below the code curve reflecting the effect of an AVT environment on fatigue and [ ]a,c for accounting for mean stress that applies to materials in a corrosive environment.

Two other mean stress models were investigated for the appropriateness of their use in providing a reasonable agreement with the expected range of initiating stress amplitudes. These were the [ ]a,c shown in Figure 4-3. With a [ ]a,c, the [

]a,c.

The assessment of the benefit of a reduction in stability ratio begins with the relationship between stability ratio and deflection. For a specific tube geometry, the displacement change is directly proportional to change in stress so that stress has the same relationship with stability ratio,

$$\left[\qquad\qquad\qquad\qquad\qquad\qquad \right]^{a,c}$$

The slope in this equation can range from [$]^{a,c}$ on a log scale depending on the amplitude of displacement. Knowing the stress resulting from a change in stability ratio from SR_1 to SR_2, the cycles to failure at the stress amplitude were obtained from the fatigue curve. A fatigue usage per year was then determined assuming continuous cycling at the natural frequency of the tube. The initial stress was determined to be in the range of 4.0 to 10.0 ksi by the fractography analysis.

It was further developed that the maximum initiating stress amplitude was not more than 9.5 ksi. This was based on [

$]^{a,c}$. The corresponding stress level is 5.6 ksi.

The maximum stress, 9.5 ksi, would be reduced to [$]^{a,c}$ with a 10% reduction in stability ratio and would have a future fatigue usage of [$]^{a,c}$ per year at 75% availability, Figure 4-4. The minimum stress, 5.6 ksi, would be reduced to [$]^{a,c}$ ksi with a 5% reduction in stability ratio and would have future fatigue usage of [$]^{a,c}$ per year, Figure 4-5. In addition, if a tube were already cracked, the crack could be as large as [$]^{a,c}$ inch in length and thru-wall and would not propagate if the stress amplitudes are reduced to $\leq$ 4.0 ksi.

Subsequent to the return to power evaluation for North Anna Unit 1, the time history of operation was evaluated on a normalized basis to the last cycle. [

]a,c, cumulative fatigue usage may then be computed to get a magnitude of alternating stress for the last cycle that results in a cumulative usage of 1.0 for the nine-year duty cycle. The result of the iterative analysis is that the probable stress associated with this fatigue curve during the last cycle of operation was approximately [ ]a,c for R9C51, North Anna Unit 1, Steam Generator C, and that the major portion of the fatigue usage came in the second, third and fourth cycles. The first cycle was conservatively omitted, since denting is assumed, for purposes of this analysis, to have occurred during that first cycle. Based on this evaluation, the tube fatigue probably occurred over most of the operating history of North Anna Unit 1.

A similar calculation can be performed for the time history of operation assuming that [

]a,c. On this basis, the effect of a 10% reduction in stability ratio is to reduce the stress amplitude to 4.0 ksi and results in a future fatigue usage of [ ]a,c.

Other combinations of alternating stress and mean stress were evaluated with -3 sigma and -2 sigma fatigue curves to demonstrate the conservatism of the 10% reduction in stability ratio. Table 4-1 presents the results of the cases analyzed clearly demonstrating that the 10% reduction in stability ratio combined with a -3 sigma fatigue curve and with maximum mean stress effects is conservative. Any higher fatigue curve whether through mean stress, mean stress model, or probability, results in greater benefit for the same reduction in stability ratio. Further, for any of these higher curves, a smaller reduction in stability ratio than 10% would result in the same benefit. In addition, there is a large benefit in terms of fatigue usage for relatively small changes in the fatigue curve.

4.2 Local Flow Peaking Considerations

Local flow peaking is a factor on stability ratio that incorporates the effects of local flow velocity, density and void fraction due to non-uniform AVB insertion depths. The flow peaking factor is applied directly to the stability ratio obtained from thermal-hydraulic analysis that does not account for these local geometry effects. Being a direct factor on stability ratio, a small percentage increase can result in a significant change in the prediction of tube response.

Since the evaluation of V. C. Summer tubing is relative to R9C51, North Anna Unit 1, the flow peaking factors are also applied as relative ratios, i.e., a ratio of V. C. Summer tubing to R9C51 at North Anna Unit 1. The flow peaking relative instability is obtained by testing in the air test rig described in Section 5.4, where the peaking factor is defined as the critical velocity for R9C51 AVB pattern compared to critical velocity for a uniform AVB pattern. As explained in Section 8.0, the minimum value of [ ]^{a,b,c} is appropriate for R9C51 of North Anna 1. The peaking factor for a tube in V. C. Summer tubing is therefore divided by [ ]^{a,b,c} and the resulting relative flow peaking is multiplied times the relative stability ratio based on ATHOS results. If the peaking factor is 1.0, the relative flow peaking is [ ]^{a,b,c}.

As a further demonstration of the conservatism of [ ]^{a,b,c} as the minimum flow peaking factor for R9C51, the stress amplitude of 7.0 ksi obtained from iterating on cumulative fatigue usage (and selected as the nominal value from fractography analysis) was used to back calculate the apparent stability ratio and then the apparent flow peaking factor. Allowing for a range of slopes of the instability curve from 10 to 30, the stability ratio is in the range of 1.1 to 1.4 and the flow peaking factor is in the range of 1.8 to 2.2. This range of flow peaking agrees with the range of flow peaking factors measured in the air tests and is considered to be the best estimate of the range of the R9C51 flow peaking factor.

The range of stability ratios, 1.1 to 1.4, is based on a value of 0.59 obtained with ATHOS results without flow peaking and with nominal damping that is a function of modal effective void fraction. The nominal damping reflects the nominal reduction in damping that occurs with denting at the tube support plate. Therefore, a minimum damping scenario that is independent of void fraction is not considered to be credible and is not addressed in the evaluation that follows.

4.3 Stress Ratio Considerations

In Section 4.1, a 10% reduction in stability ratio was established to reduce the stress amplitude on the Row 9 Column 51 tube of North Anna Unit 1 to a level that would not have ruptured, 4.0 ksi. To apply this same criteria to another tube in the same or another steam generator, the differences in [

]a,c.

a,c

[ ]

a,c

where the stability ratio (SR) includes the flow peaking effect.

By est. blishing their equivalent effect on the stress amplitude produced the tube rupture at North Anna 1, several other effects may be accounted for. These include a lower mean stress (such as for non-dented tubes), different frequency tubes from the [ ]^{a,c,e} hertz frequency of R9C51, North Anna 1, and shorter design basis service.

In the case of lower mean stress, the stress amplitude that would have caused the failure of R9C51, North Anna 1, would have been higher. [

]^{a,c}.

A lower or higher frequency tube would not reach a usage of 1.0 in the same length of time as the R9C51 tube due to the different frequency of cycling. The usage accumulated is proportional to the frequency and, therefore, the allowable number of cycles to reach a usage of 1.0 is inversely proportional to frequency. The equivalent number of cycles to give the usage of 1.0 for a different frequency tube [

]^{a,c}.

For a different time basis for fatigue usage evaluation, [

]^{a,c,e}.

Knowing the magnitude of the stress ratio allows 1) the determination of tubes that do not meet a value of ≤ 1, and 2) the calculation of maximum stress in the acceptable tubes,

$$\left[\qquad\qquad\qquad\right]^{a,c}$$

Having this maximum stress permits the evaluation of the maximum fatigue usage for V. C. Summer based on the time history expressed by normalized stability ratios for the duty cycle (see Section 7.4).

Table 4-1

Fatigue Usage per Year Resulting

From Stability Ratio Reduction

SR, % REDUCTION	STRESS BASIS(1)	FATIGUE CURVE(2)	MEAN STRESS MODEL	USAGE PER YEAR
5.	9 yrs to fail [ ]a,c	[		]a,c
5.	9 yrs to fail [ ]a,c			
5.	9 yrs to fail [ ]a,c			
10.	max. stress amplitude(4) [ ]a,c			
10.	max. stress amplitude(4) [ ]a,c			
10.	max. stress amplitude(4) [ ]a,c			
10.	max. stress amplitude(4) [ ]a,c			
10.	max. stress based on duty cycle(5) [ ]a,c			]

(1) This gives the basis for selection of the initiating stress amplitude and its value in ksi.

(2) S_m is the maximum stress applied with $S_m = S_{mean} + S_a$

(3) [ ]a,c.

(4) Cycles to failure implied by this combination of stress and fatigue properties is notably less than implied by the operating history. Consequently this combination is a conservative, bounding estimate.

(5) Cycles to failure implied by the operating history requires [ ]a,c fatigue curve at the maximum stress of [ ]a,c.

a,b,c

Figure 4-1 Vibration Displacement vs. Stability Ratio

a,c

[ ]

Figure 4-2 Fatigue Strength of Inconel 600 in AVT Water at 600°F

a,c

[ ]

Figure 4-3 Fatigue Curve for Inconel 600 in AVT Water
Comparison of Mean Stress Correction Models

a,c

Figure 4-4 Modified Fatigue with 10% Reduction in Stability Ratio for Maximum Stress Condition

a,c

Figure 4-5 Modified Fatigue with 5% Reduction in Stability Ratio for Minimum Stress Condition

5.0 SUPPORTING TEST DATA

This section provides a mathematical description of the fluidelastic mechanism, was determined to be the most likely causative mechanism for the North Anna tube rupture, as discussed in Section 3.3, to highlight the physical conditions and corresponding parameters directly related to the event and associated preventative measures. The basis for establishing the appropriate values and implications associated with these parameters are provided. Where appropriate, test results are presented.

5.1 Stability Ratio Parameters

Fluidelastic stability ratios are obtained by evaluations for specific configurations, in terms of active tube supports, of a specific tube. These stability ratios represent a measure of the potential for tube vibration due to instability during service. Fluidelastic stability evaluations are performed with a computer program which provides for the generation of a finite element model of the tube and tube support system. The finite element model provides the vehicle to define the mass and stiffness matrices for the tube and its support system. This information is used to determine the modal frequencies (eigenvalues) and mode shapes (eigenvectors) for the linearly supported tube being considered.

The methodology is comprised of the evaluation of the following equations:

Fluidelastic stability ratio = SR = U_{en}/U_c for mode n,

where U_c (critical velocity) and U_{en} (effective velocity) are determined by:

$$U_c = \beta\, f_n\, D\, [(m_o\, \delta_n) / (\rho_o\, D^2)]^{1/2} \qquad [1]$$

and;

$$U_{en}^2 = \frac{\sum_{j=1}^{N} (\rho_j/\rho_o)\, U_j^2 \phi_{jn}^2\, z_j}{\sum_{j=1}^{N} (m_j/m_o)\, \phi_{jn}^2\, z_j} \qquad [2]$$

where,

D = tube outside diameter, inches

U_{en} = effective velocity for mode n, inches/sec

N = number of nodal points of the finite element model

m_j, U_j, ρ_j = mass per unit length, crossflow velocity and fluid density at node j, respectively

ρ_o, m_o = reference density and a reference mass per unit length, respectively (any representative values)

δ_n = logarithmic decrement (damping)

ϕ_{jn} = normalized displacement at node j in the nth mode of vibration

z_j = average of distances between node j to j-1, and j to J+1

β = an experimentally correlated stability constant

Substitution of Equations [1] and [2] into the expression which defines stability ratio, and cancellation of like terms, leads to an expression in fundamental terms (without the arbitrary reference mass and density parameters). From this resulting expression, it is seen that the stability ratio is directly related to the flow field in terms of the secondary fluid velocity times square-root-density distribution (over the tube mode shape), and inversely related to the square root of the mass distribution, square root of modal damping, tube modal frequency, and the stability constant (beta).

The uncertainty in each of these parameters is addressed in a conceptual manner in Figure 5-1. The remainder of this section (Section 5.0) provides a discussion, and, where appropriate, the experimental bases to quantitatively establish the uncertainty associated with each of these parameters. In addition, Section 5.3 provides the experimental basis to demonstrate that tubes with [ ]^{a,c}. This implies that those tubes [ ]^{a,c} would not have to be modified because their instability response amplitude (and stress) would be small. The very high degree of sensitivity of tube response (displacements and stresses) to changes in the velocity times square-root-density distribution is addressed in Section 4.0. This is important in determining the degree of change that can be attained through modifications.

Frequency

It has been demonstrated by investigators that analytically determined frequencies are quite close to their physical counterparts obtained from measurements on real structures. Thus, the uncertainty in frequencies has been shown to be quite small. This is particularly appropriate in the case of dented (fixed boundary condition) tubes. Therefore, uncertainty levels introduced by the frequency parameter are expected to be insignificant (see also "Average Flow Field" subsection below).

Instability Constant (Beta)

The beta (stability constant) values used for stability ratio and critical velocity evaluations (see above equations) are based on an extensive data base comprised of both Westinghouse and other experimental results. In addition, previous field experiences are considered. Values have been measured for full length U-bend tubes in prototypical steam/water environments. In addition, measurements in U-bend air models have been made with both no AVB and variable AVB supports (Figure 5-3).

To help establish the uncertainties associated with ATHOS flow velocity and density distribution predictions on stability analyses, the Model Boiler (MB-3) tests performed at Mitsubishi Heavy Industries (MHI) in Japan were modeled using ATHOS. A beta value consistent with the ATHOS predicted flow conditions and the MB-3 measured critical velocity was determined. These analyses supported a beta value of [ ]^{a,b,c}.

A summary of the test bases and qualifications of the beta values used for these assessments is provided by Figure 5-2. The lowest measured beta for tubes without AVBs was a value of [ ]^{a,b,c}. This value is used for the beta parameter in all stability ratio evaluations addressed in this Report (see also "Average Flow Field" subsection below).

Mass Distribution

The mass distribution parameter is based on known information on the tube and primary and secondary fluid physical properties. The total mass per unit length is comprised of that due to the tube, the internal (primary) fluid, and the external (secondary) fluid (hydrodynamic mass). Data in Reference 5-2 suggests that at operating void fractions [

]^{a,c}.

Tube Damping

Test data are available to define tube damping for clamped (fixed) tube supports, appropriate to dented tube conditions, in steam/water flow conditions. Prototypic U-bend testing has been performed under conditions leading to pinned supports. The data of Axisa in Figure 5-4 provides the principal data for clamped tube conditions in steam/water. This data was obtained for cross flow over straight tubes. Uncertainties are not defined for the data from these tests. Detailed tube damping data used in support of the stability ratio evaluations addressed in this report are provided in Section 5.2, below.

Flow Field - Velocity Times Square-Root-Density Distribution

Average and U-bend-local flow field uncertainties are addressed independently in the following.

Average Flow Field

Uncertainties in the average flow field parameters, obtained from ATHOS analyses, coupled with stability constant and frequency, are essentially the same for units with dented or non-dented top support plates. If the errors associated with these uncertainties were large, similar instabilities would be expected in the non-dented units with resulting wear at either the top support plate or inner row AVBs. Significant tube wear has not been observed in inner row tubes in operating steam generators without denting. Thus, an uncertainty estimate of about [ ]^{a,c} for the combined effects of average flow field, stability constant and frequency appears to be reasonable. To further minimize the impact of these uncertainties, the V. C. Summer tubes are evaluated on a relative basis, so that constant error factors are essentially eliminated. Thus, the uncertainties associated with the average velocity times square-root-density (combined) parameter are not expected to be significant.

U-Bend Local Flow Field

Non-uniform AVB insertion depths have been shown to have effects on stability ratios. Flow peaking, brought about by the "channeling" effects of non-uniform AVBs, leads to a local perturbation in the velocity times square-root-density parameter at the apex of the tube where it will have the largest effect (because the apex is where the largest vibration displacements occur). Detailed local flow field data used in support of the stability ratio evaluations addressed in this report are provided in Section 5.2, below.

Overall Uncertainties Assessment

Based on the above discussions, and the data provided in the following sections, it is concluded that local flow peaking is likely to have contributed significantly to the instability and associated increased vibration amplitude for the failed North Anna tube. Ratios of stresses and stability ratios relative to the North Anna tube, R9C51, are utilized in this report to minimize uncertainties in the evaluations associated with instability constants, local flow field effects and tube damping.

5.2 Tube Damping Data

The damping ratio depends on several aspects of the physical system. Two primary determinants of damping are the support conditions and the flow field. It has been shown that tube support conditions (pinned vs clamped) affect the damping ratio significantly. Further, it is affected by the flow conditions, i.e., single-phase or two-phase flow. These effects are discussed below in more detail.

Reference (5-1) indicates that the damping ratio in two phase flow is a sum of contributions from structural, viscous, flow-dependent, and two-phase damping. The structural damping will be equal to the measured damping in air. However, in two-phase flow, the damping ratio increases significantly and is dependent on the void fraction or quality. It can be shown that the damping contribution from viscous effects are very small.

Damping ratios for tubes in air and in air-water flows have been measured and reported by various authors. However, the results from air-water flow are poor representations of the actual conditions in a steam generator (steam-water flow at high pressure). Therefore, where available, results from prototypic steam-water flow conditions should be used. Fortunately, within the past few years test data on tube vibration under steam-water flow has been developed for both pinned and clamped tube support conditions.

Two sources of data are particularly noteworthy and are used here. The first is a large body of recent, as yet unpublished data from high pressure steam-water tests conducted by Mitsubishi Heavy Industries (MHI). These data were gathered under pinned tube support conditions. The second is comprised of the results from tests sponsored by the Electric Power Research Institute (EPRI) and reported in References (5-2) and (5-3).

The damping ratio results from the above tests are plotted in Figure 5-4 as a function of void fraction. It is important to note that the void fraction is determined on the basis of [ ]a,c

(Reference (5-4)). The upper curve in the figure is for pinned support conditions. This curve represents a fit to a large number of data points not shown in the figure. The points on the curve are only plotting aids, rather than specific test results.

The lower curve pertains to the clamped support condition, obtained from Reference (5-3). Void fraction has been recalculated on the basis of slip flow. It may be noted that there is a significant difference in the damping ratios under the pinned and the clamped support conditions. Damping is much larger for pinned supports at all void fractions. Denting of the tubes at the top support plate effectively clamps the tubes at that location. Therefore, the clamped tube support curve is used in the current evaluation to include the effect of denting at the top tube support plate.

The Reference 5-3 data as reported show a damping value of .5% at 100% void fraction. The 100% void fraction condition has no two phase damping and is considered to be affected principally by mechanical or structural damping. Westinghouse tests of clamped tube vibration in air have shown that the mechanical damping is only [ ]^{a,c} rather than the 0.5% reported in Reference (5-3). Therefore the lower curve in Figure 5-4 is the Reference (5-3) data with all damping values reduced by [ ]^{a,c}.

5.3 Tube Vibration Amplitudes With Single-Sided AVB Support

A series of wind tunnel tests were conducted to investigate the effects of tube/AVB eccentricity on the vibration amplitudes caused by fluidelastic vibration.

[

]^{a,c}. Prior test results obtained during the past year using this apparatus have demonstrated that the fluidelastic vibration characteristics observed in the tests performed with the cantilever tube apparatus are in good agreement with corresponding characteristics observed in wind tunnel and steam flow tests using U-bend tube arrays. A summary of these prior results is given in Table 5-1.

An overall view of the apparatus is shown in Figure 5-5. Figure 5-6 is a top view of the apparatus. [

]^{a,c}.

As shown in Figure 5-7, the tube vibration amplitude below a critical velocity is caused by [

]^{a,c}.

Figure 5-7 shows the manner in which the zero-to-peak vibration amplitude, expressed as a ratio normalized to [ ]^{a,c}, varies when one gap remains at [ ]^{a,c}. For increasing velocities, up to that corresponding to a stability ratio of [

]^{a,c}. Figure 5-8 shows typical vibration amplitude and tube/AVB impact force signals corresponding to those obtained from the tests which provided the results shown in Figure 5-7. As expected, impacting is only observed in the [ ]^{a,c}.

It is concluded from the above test results that, [

]^{a,c}.

5.4 Tests to Determine the Effects on Fluidelastic Instability of Columnwise Variations in AVB Insertion Depths

This section summarizes a series of wind tunnel tests that were conducted to investigate the effects of variations in AVB configurations on the initiation of fluidelastic vibration. Each configuration is defined as a specific set of insertion depths for the individual AVBs in the vicinity of an unsupported U-bend tube.

The tests were conducted in the wind tunnel using a modified version of the cantilever tube apparatus described in Section 5.3. Figure 5-9 shows the conceptual design of the apparatus. The straight cantilever tube, [

]^{a,c}.

[

]^{a,c}. Figure 5-11 shows the AVBs, when the side panel of the test section is removed. Also shown is the top flow screen which is [

]^{a,c}. The AVB configurations tested are shown in Fig. 5-12. Configuration 1a corresponds to tube R9C51, the failed tube at North Anna. Configuration 2a corresponds to one of the cases in which the AVBs are inserted to a uniform depth and no local velocity peaking effects are expected.

As shown in Figure 5-9, [

]^{a,c}.

All the tubes except the instrumented tube (corresponding to Row 10) are [$]^{a,c}$. As discussed in Section 5.3, prior testing indicates that this situation provides a valid model. The instrumented tube [$]^{a,c}$ as shown in Figure 5.10. Its [$]^{a,c}$ direction vibrational motion is measured using a non-contacting transducer.

[

$]^{a,c}$. The instrumented tube corresponds to a Row 10 tube as shown in Figure 5-9. However, depending on the particular AVB configuration, it can reasonably represent a tube in Rows 8 through 11. The AVB profile in the straight tube model is the average of Rows 8 and 11. The difference in profile is quite small for these bounding rows.

[$]^{a,c}$ using a hot-film anemometer located as shown in Figure 5-9.

Figure 5-13 shows the rms vibration amplitude, as determined from PSD (power spectral density) measurements made using an FFT spectrum analyzer, versus flow velocity for Configuration 1a. Configuration 1a corresponds to the final, evaluated positions of AVBs near tube R9C51 in North Anna (See Figures 8-6 and 8-7). Data for three repeat tests are shown and the critical velocity is identified. The typical rapid increase in vibration amplitude when the critical velocity for fluidelastic vibration is exceeded is evident.

The main conclusions from the tests are:

1. Tube vibration below the critical velocity is relatively small, typical of turbulence-induced vibration, and increases rapidly when the critical velocity for the initiation of fluidelastic vibration is exceeded.

2. Configuration 1b (which was initially thought to represent AVB positions near R9C51 in North Anna until re-evaluation indicated Configuration 1a) has the lowest critical velocity of all the configurations tested.

3. Configuration 1b is repeatable and the configuration was rerun periodically to verify the consistency of the test apparatus.

The initial test results obtained in support of the V. C. Summer evaluation are summarized in Table 5-2. The test data are presented as velocity peaking ratios, the ratio of critical velocity for North Anna tube R9C51 configuration 1a, to that for each V. C. Summer AVB configuration evaluated.

5.5 References

a,b,c

Table 5-1

Wind Tunnel Tests on Cantilever Tube Model

OBJECTIVE: Investigate the effects of tube/AVB fitup on flow-induced tube vibration.

APPARATUS: Array of cantilevered tubes with end supports [

]a,c.

MEASUREMENTS: Tube vibration amplitude and tube/AVB impact forces or preload forces.

RESULTS:

a,b,c

[

]

Table 5-2

Fluidelastic Instability Velocity Peaking Ratios for Columnwise Variation in AVB Insertion Depths (V. C. Summer)

Type of Insertion Configuration	Peaking Ratio U_{1a}/U_n
	a,b,c
1a	
1b	
1k	
1w	
1x	
1y	
2a	
4a	
4b	
4c	
4d	
4o	
4x	
5a	
5b	
5c	
8p	
8q	

Note: U_n is instability velocity at inlet for type n of AVB insertion configuration.

a,c

Figure 5-1 Fluidelastic Instability Uncertainty Assessment

U-Bend Test Data

1) MB-3 Tests

   β values of [ ]^{a,b,c}

2) MB-2 Tests

   β of [ ]^{a,b,c}

3) Air Model Tests

   β of [ ]^{a,b,c} without AVBs

   Tendency for β to increase in range of [ ]^{a,b,c} with inactive AVBs (gaps at AVBs)

   Tendency for β to decrease toward a lower bound of [ ]^{a,b,c} with active AVBs

Verification of Instability Conditions

1) Flow conditions at critical velocity from MB-3
2) Measured damping for the specific tube
3) Calculated velocities from ATHOS 3D analysis
4) β determined from calculated critical values
   Good agreement with reported β values
5) ATHOS velocity data with β of [ ]^{a,b,c} and known damping should not significantly underestimate instability for regions of uniform U-bend flow

Figure 5-2 Instability Constant - β

a,b,c

Figure 5-3 Instability Constants, β, Obtained for Curved Tubes from Wind Tunnel Tests on the 0.214 Scale U-Bend Model

a,b,c

Figure 5-4 Damping vs. Slip Void Fraction

a,b,c

Figure 5-5 Overall View of Cantilever Tube Wind Tunnel Model

a,b,c

Figure 5-6 Top View of the Cantilever Tube Wind Tunnel Model

25368-2

a,b,c

Figure 5-7 Fluidelastic Vibration Amplitude with Non-Uniform Gaps

a,b,c

Figure 5-8 Typical Vibration Amplitude and Tube/AVB Impact Force Signals for Fluidelastic Vibration with Unequal Tube/AVB Gaps

a,b,c

Figure 5-9 Conceptual Design of the Apparatus for Determining the Effects of Fluidelastic Instability of Columnwise Variations in AVB Insertion Depths

a,b,c

Figure 5-10 Overall View of Wind Tunnel Test Apparatus

a,b,c

Figure 5-11 Side View of Wind Tunnel Apparatus with Cover Plates Removed to Show Simulated AVBs and Top Flow Screen

25368-4

TYPE OF AVB INSERTION	TYPE OF AVB INSERTION
a, c	a, c

Figure 5-12 AVB Configurations Tested for V. C. Summer

a,b,c

Figure 5-13 Typical Variation of RMS Vibration Amplitude with Flow Velocity for Configuration 1a in Figure 5-12

6.0 EDDY CURRENT DATA AND AVB POSITIONS

From the eddy current tapes provided by SCE&G for the October 1988 inspection of the V. C. Summer steam generators, Westinghouse performed a review of eddy current signals in the U-bend region. Approximately 1700 eddy current traces in locations in Rows 7 through 16 were analyzed for the presence of signals indicating AVBs. In addition, twenty-five (25) tubes with potential local flow field effects were examined for the presence of denting.

6.1 V. C. Summer AVB Assembly Design

[

]^{a,c,e} Review of the EC data for V. C. Summer shows that AVB insertion depth is fairly uniform in the regions between Columns 31 and 84 (corresponding to the "flat" contour of the tube bundle in this region) with insertion depth in most cases to Row 9 or lower. AVB insertion depth in the remainder of the columns is more variable, tending to a higher depth of insertion.

6.2 Eddy Current Data for AVB Positions

The AVB insertion depths were determined on the basis of interpretation of the eddy current data. To locate the AVBs, the ECT data traces were searched for the characteristic peaks seen in the signals which indicate the intersection of an AVB (or a tube support plate) with the tube (Figure 6-1). Since ambiguity can occur in the interpretation of the ECT data, due to inability of

ECT to differentiate on which side of a tube a "visible" AVB is located, other information was used to assist in establishing the location of the AVBs. [

]^{a,c}

The number of these AVB intersections, including zero (meaning no AVB present), was evaluated for each tube to indicate the presence or absence of AVBs. Figures 6-2 through 6-4 show a representation of AVB insertion distance based on evaluation of the EC data. All inspected tubes in these figures, with the exception of those indicated with a "0" or a "1", have two or more "visible" AVB signals. In cases where no AVBs were indicated, a "0" is shown, and likewise, a "1" is shown where "one AVB" is indicated.

The direct observation data (the number of AVB intersections seen by the eddy current probe) are the principal basis for determining the AVB positions. Where the direct observations are ambiguous or there is a conflict between observations and projections, the more conservative data are used to determine the AVB positions. Since 'direct observation' gives a 'yes - no' type of answer, the projection method is used to 'interpolate' AVB insertion depths between rows of tubes. Greater conservatism is generally interpreted as the AVB being less inserted although consideration must also be given to the resulting flow peaking factors.

In the case where the AVB characteristic signals can not be confidently determined due to a noisy signal or pre-existing plugged tubes, location data for the AVBs is provided for [

]a,c

6.3 Tube Denting at Top Tube Support Plate

Subsequent to identifying the AVB signals, the Eddy Current (EC) tapes were evaluated [ ]a,c to determine the condition of the tube/top tube support interface of the unsupported tubes having potential flow peaking. Because of the significance of the top tube support plate crevice conditions on the analysis and the potential for further corrosion at the top tube support plate since the October 1988 EC inspection, the EC analysis assumed the top tube support plate crevices to be dented (i.e. having "corrosion with magnetite" or "tube denting with deformation") unless they could conclusively be demonstrated to be otherwise. Analyses of eddy current (EC) data for V. C. Summer showed the presence of "corrosion with magnetite" in roughly half of the tube/TSP crevices. Of the twenty-five (25) tube eddy current results from the October, 1988, inspection that were evaluated for top tube support plate corrosion, eleven (11) were found to be magnetite packed at one or both top tube support plate legs, none showed denting with deformation, and the remaining fourteen (14) showed no detectable magnetite or corrosion. For conservatism in the evaluation, all of the tubes evaluated are postulated to be dented. The effect of denting on the fatigue usage of the tube has been conservatively maximized by assuming the maximum effect of mean stress in the tube fatigue usage evaluation and by incorporating reduced damping in the tube vibration evaluation.

6.4 AVB Map Interpretations

6.4.1 Description by Steam Generator

To review the relationship of tube stability and tube row number, it is useful to examine Figure 9-8, at the end of Section 9. This figure combines the effects of the tube position (row and column), tube bundle flow-field (velocities, densities, and damping), and tube geometry (bend radius, etc.) to develop an allowable flow peaking ratio for each tube. The allowable flow peaking ratio is the highest flow peaking factor that a particular tube may experience before exceeding a stress ratio of 1.0 as compared to the North Anna R9C51, previously established in Section 4.0. Changes in the flow field account for some of the variation in the allowable peaking ratio, and the peripheral tubes (Column 2) can accept higher peaking ratios, since their allowables are determined from an approach velocity developed from a square-root-sum-of-the-squares formulation of the gap velocity on one side of the tube and the comparatively low bulk flow velocity on the periphery. Observing the variation in allowable flow peaking versus row number, a [ ]^{a,c} decrease in the allowable flow peaking factor per row can be seen. Since a flow peaking ratio of 1.0 indicates that the flow peaking factor for the tube being examined is identical to that of North Anna R9C51, it can be seen from Figure 9-8 that nearly all V. C. Summer Row 9 tubes would require a peaking factor equivalent or greater than North Anna R9C51 to exceed the stability ratio criteria.

SG-A

The AVB map is given in Figure 6-2. All Row 12, Row 11 and Row 10 tubes are supported. Thirty-eight (38) Row 9 tubes, ninety-four (94) Row 8 tubes, and one hundred and nine (109) Row 7 tubes are unsupported. AVB insertion depths vary slightly from Column 2 through Column 30, gradually from Column 31 to Column 81, and to a greater extent between Columns 82 and 113.

R9C83 is the highest loaded tube in this steam generator, having a relative stability ratio, including the effects of local flow peaking, of [

]. ^{a,c} No appreciable magnetite was evaluated as being present in the top tubes support plate cre\ .ces of this tube, based upon a review of the October 1988 eddy current tapes.

The AVB positions near R9C83 [

]^{a,c}

AVB insertion depths near SG-A R8C11 were evaluated to determine the potential for flow peaking. Based on the [

]^{a,c} With this conservative arrangement of AVBs, SG-A R8C11 is evaluated to have no flow peaking.

Insertion depths near SG-A R8C92 were also evaluated to determine the potential for flow peaking. Based on the [

]^{a,c} With this insertion depth, as shown in Figure 6-2, SG-A R8C92 is evaluated to have no flow peaking. In the unlikely event that [

]^{a,c}

Of the remaining tubes in SG-A, R9C55 is the highest loaded. This tube has a flow peaking ratio of [ ]^{a,c} Flow peaking factor selections for all tubes having significant relative stability ratios or stress ratios are discussed in Section 8.8.

SG-B

The AVB map is given in Figure 6-3. All Row 12, Row 11 and Row 10 tubes are supported. Four (4) Row 9 tubes, sixty-three (63) Row 8 tubes, and ninety-nine (99) Row 7 tubes are unsupported. AVB insertion depths vary gradually from Column 3 to Column 31 and from Column 84 to Column 113. Insertion depths generally vary slightly Column 32 to Column 83, except for a depth variation between Columns 50-60.

R9C56 is the highest loaded tube in this steam generator, having a relative stability ratio, including the effects of local flow peaking, of [

]^{a,c} Based upon a review of the October 1988 eddy current tapes, magnetite was evaluated as being present at the top hot leg tube support plate crevice of this tube, and no appreciable magnetite was evaluated as being present on the cold leg top tube support plate crevice.

The AVB positions near R9C56 [

]^{a,c}

Of the remaining tubes in SG-B, R9C110 is the highest loaded. This tube has a flow peaking ratio of [

]^{a,c} Flow peaking factor selections for other, lower row tubes are reviewed in Section 8.8.

SG-C

The AVB map is given in Figure 6-4. No Row 14, one Row 13, and one Row 12 tubes are unsupported. Five (5) Row 11 tubes, twelve (12) Row 10 tubes, twenty-eight (28) Row 9 tubes, forty-eight (48) Row 8 tubes, and one hundred and five (105) Row 7 tubes are unsupported. AVB insertion depths vary significantly from Column 2 to Column 31, slightly from Column 32 to Column 83, and gradually from Column 84 to 113.

R13C5 is the highest loaded tube in this steam generator, having a relative stability ratio including the effects of local flow peaking [ ][a,c] Other tubes having significant relative stability ratios are R12C5 [ ][a,c]; R10C23 [ ];[a,c] R9C29 [ ][a,c]; and R9C106 [ ][a,c] All five of the above listed tubes underwent ameliorative action [ ].[a,c] The flow peaking factor selected for R13C5 is [ ].[a,c] This is higher than the 1.47 flow peaking factor determined for North Anna R9C51, and gives a relative flow peaking ratio of [ ].[a,c] Based upon a review of the October 1988 eddy current tapes, no magnetite was evaluated as being present at the top hot leg tube support plate crevice of R13C5, R12C5 and R9C106. Magnetite signals were indicated at both tube support plate crevices of R10C23 and in the cold leg crevice of R9C29.

To account for [

].[a,c]

The AVB positions near Column 23 were [

$]^{a,c}$ and is acceptable for continued operation as described in Section 9. Tube R10C23 underwent ameliorative action.

The AVB [

$]^{a,c}$

The positions of AVBs C105/106 and C106/107 were both determined [

$]^{a,c}$ tube R10C106, resulting in the flow peaking factor described in Section 8.8.

The AVB projections near R9C106 were in good agreement, and a [
$]^{a,c}$

Of the remaining tubes in SG-C, R11C4 through R11C8 are the highest loaded. These tubes have [
$]^{a,c}$ value for these row and column numbers. Flow peaking factor selections for other, lower row tubes are reviewed in Section 8.8.

6.4.2 Summary of Support Conditions

Tubes which were evaluated as having "1" AVB signals, and determined to be supported based upon projection data and adjacent tube checks are listed in Table 6-1. With the exception of tubes listed in Table 6-2, "1 AVB Signals Indicating Support for Flow Peaking Analysis", all tubes which are drawn with an AVB inserted to a depth even with the tube centerline are supported. The tubes in Table 6-2, although unsupported, are less limiting than neighboring tubes in which flow peaking is produced, and therefore are generally not included among the "significant" tubes in Section 9, Table 9-2. Table 6-3, which includes those tubes listed in Table 6-2, provides a summary listing of all unsupported tubes. The AVB projections shown are in nearly all instances the projected values from the tube in the next highest row in a particular column. If the projection from a particular next highest row tube varies significantly with those adjacent and higher row tubes, possibly due to a signal from a deposit, all surrounding data are analyzed, and a revised projection value determined.

TABLE 6-1

V. C. Summer
1 AVB Signals Determined to be Supported

V. C. Summer Steam Generator A

Row 12	None
Row 11	None
Row 10	None
Row 9	Columns 3, 4, 109
Row 8	None
Row 7	Columns 28, 29

V. C. Summer Steam Generator B

Row 12	None
Row 11	None
Row 10	None
Row 9	Column 113
Row 8	Columns 98
Row 7	None

V.C. Summer Steam Generator C

Row 12	Column 4, 6, 7, 8
Row 11	Columns 2, 3, 4
Row 10	Columns 103, 108
Row 9	Column 28
Row 8	None
Row 7	Column 26

TABLE 6-2

1 AVB Signal Indicating Support for Flow Peaking Analysis

V. C. Summer Steam Generator A

Row 12	None
Row 11	None
Row 10	None
Row 9	None
Row 8	None
Row 7	Column 87

V. C. Summer Steam Generator B

Row 12	None
Row 11	None
Row 10	None
Row 9	None
Row 8	Columns 42
Row 7	None

V. C. Summer Steam Generator C

Row 12	None
Row 11	Column 4
Row 10	None
Row 9	None
Row 8	None
Row 7	None

TABLE 6-3

V. C. Summer Unsupported Tube Summary

V. C. Summer Steam Generator A

Row 12	None
Row 11	None
Row 10	None
Row 9	Columns 2, 5, 6, 52-83, 111-113
Row 8	Columns 2-12, 15-23, 31-84, 91-100, 104-113
Row 7	Columns 2-27, 30-85, 87-113

V. C. Summer Steam Generator B

Row 12	None
Row 11	None
Row 10	None
Row 9	Columns 56, 109-111
Row 8	Columns 2-8, 32-42, 44-50, 55-80, 96, 97, 104-113
Row 7	Columns 2-12, 15-24, 27, 31-84, 91-113

V. C. Summer Steam Generator C

Row 14	None
Row 13	Column 5
Row 12	Column 5
Row 11	Columns 4-8
Row 10	Columns 2-8, 11, 12, 23, 106, 113
Row 9	Columns 2-8, 11-13, 16-20, 23, 27-29, 105-113
Row 8	Columns 2-20, 23, 24, 27-30, 53-55, 92-113
Row 7	Columns 2-20, 23, 24, 27-84, 88-113

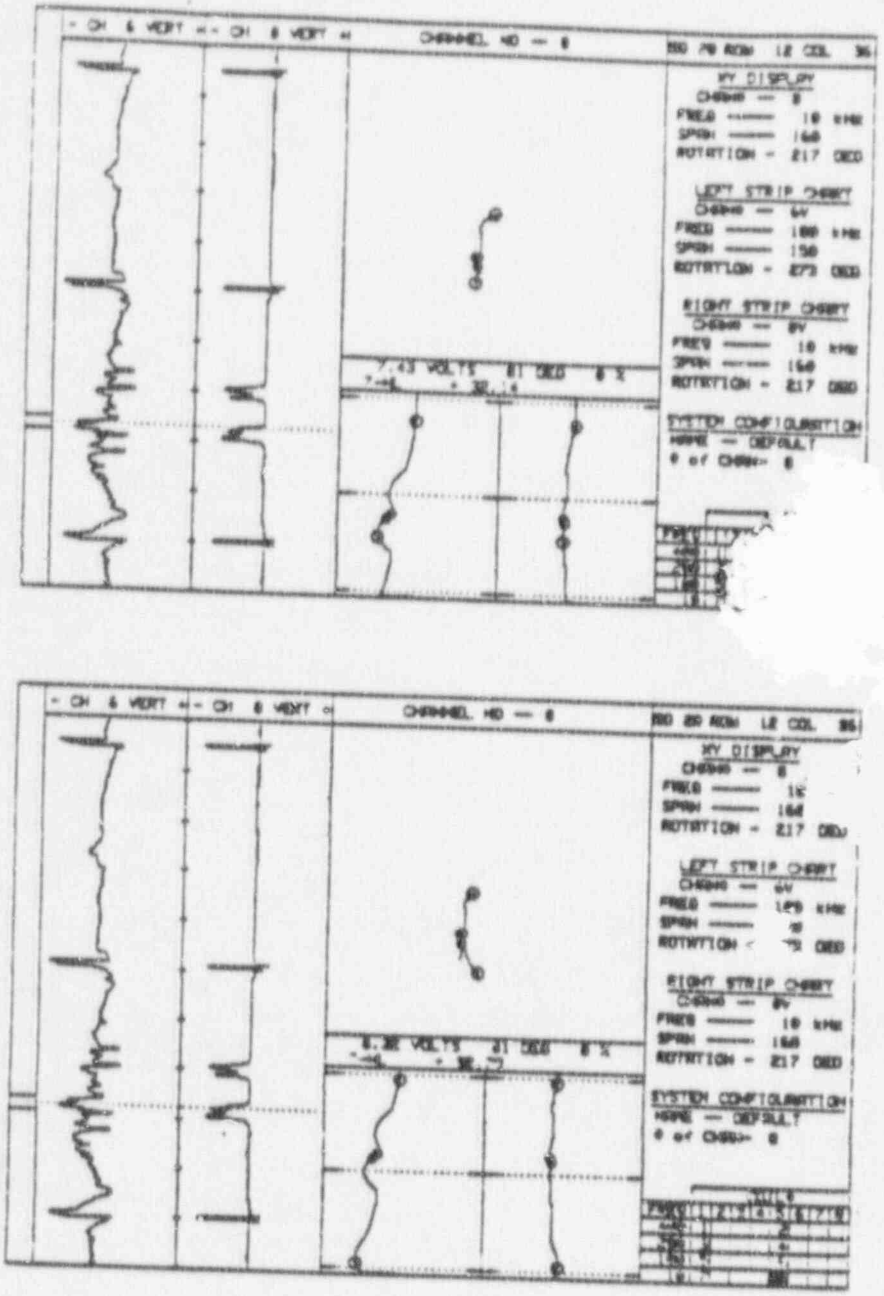

Figure 6-1 AVB Insertion Depth Confirmation

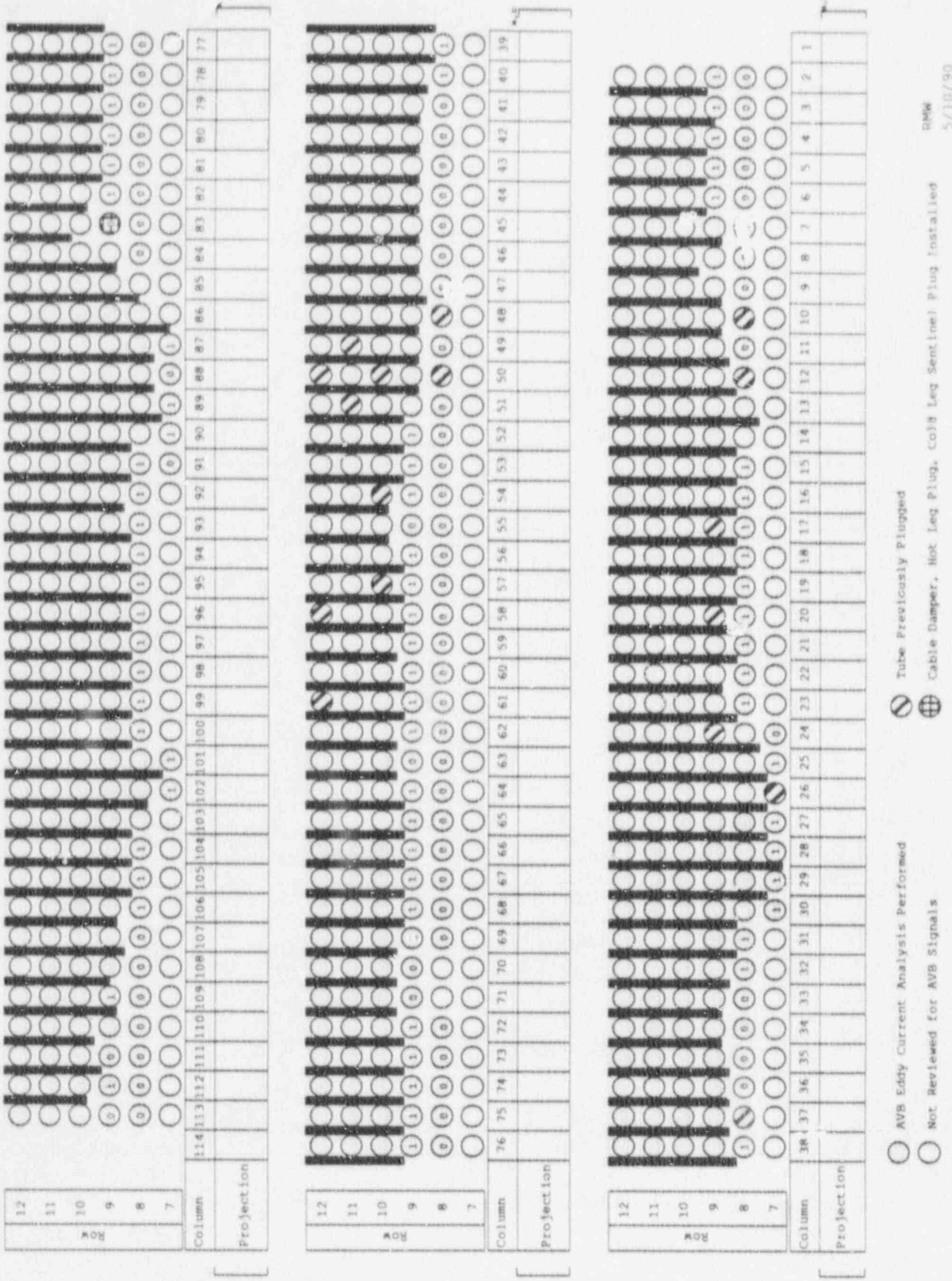

Figure 6-2 V. C. Summer Steam Generator A AVB Positions

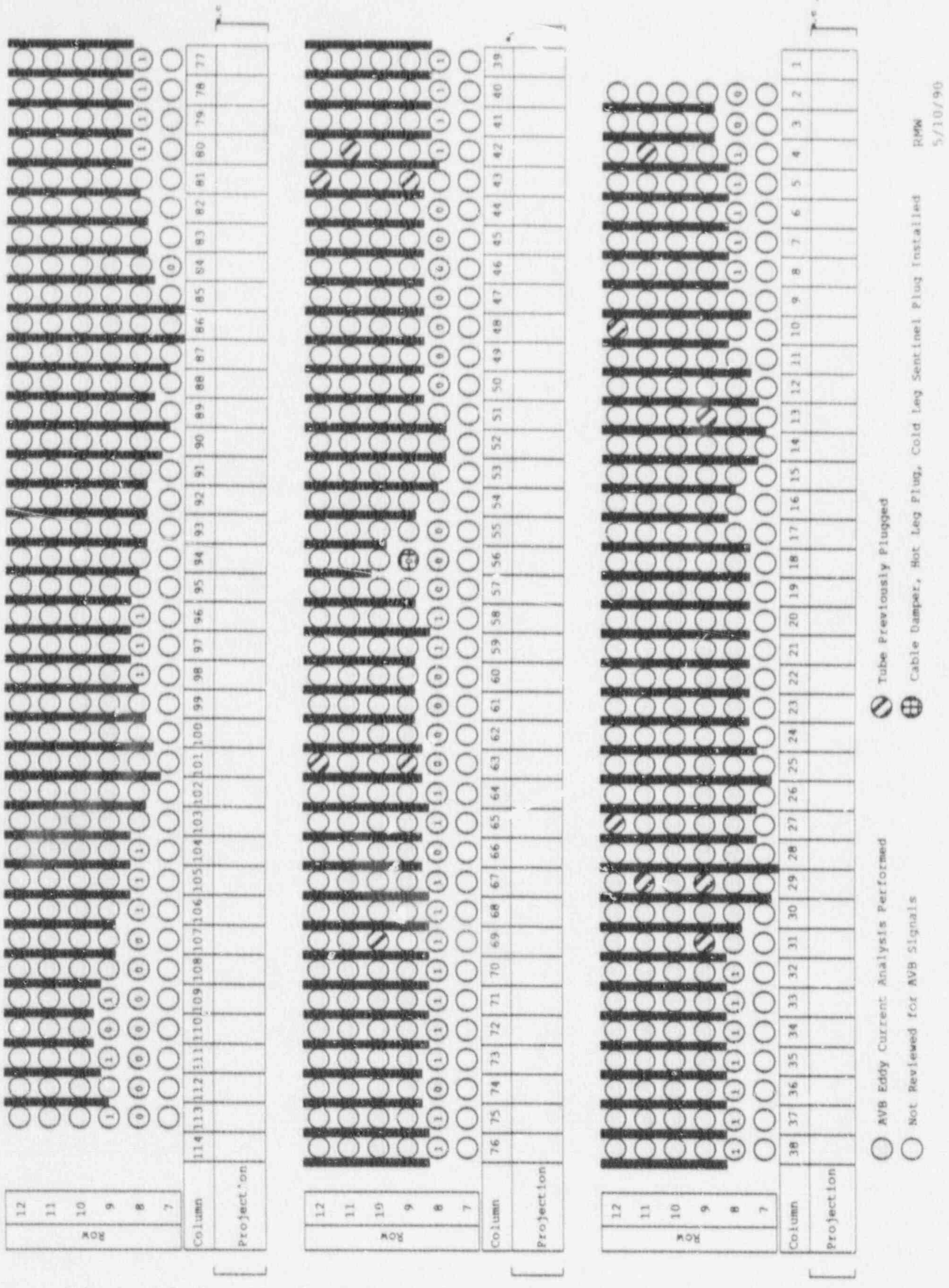

Figure 6-3 V. C. Summer Steam Generator B AVB Positions

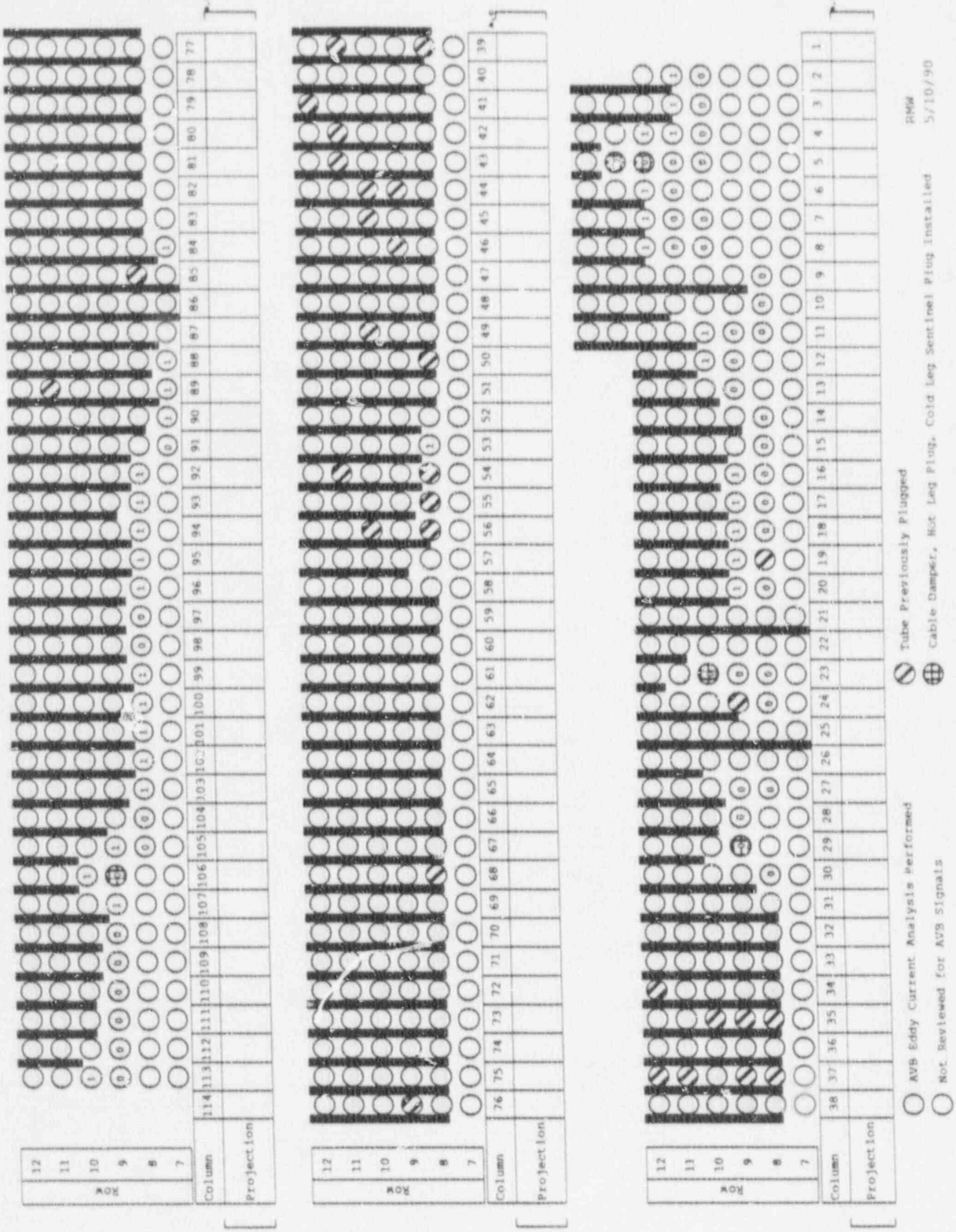

Figure 6-4 V. C. Summer Steam Generator C AVB Positions

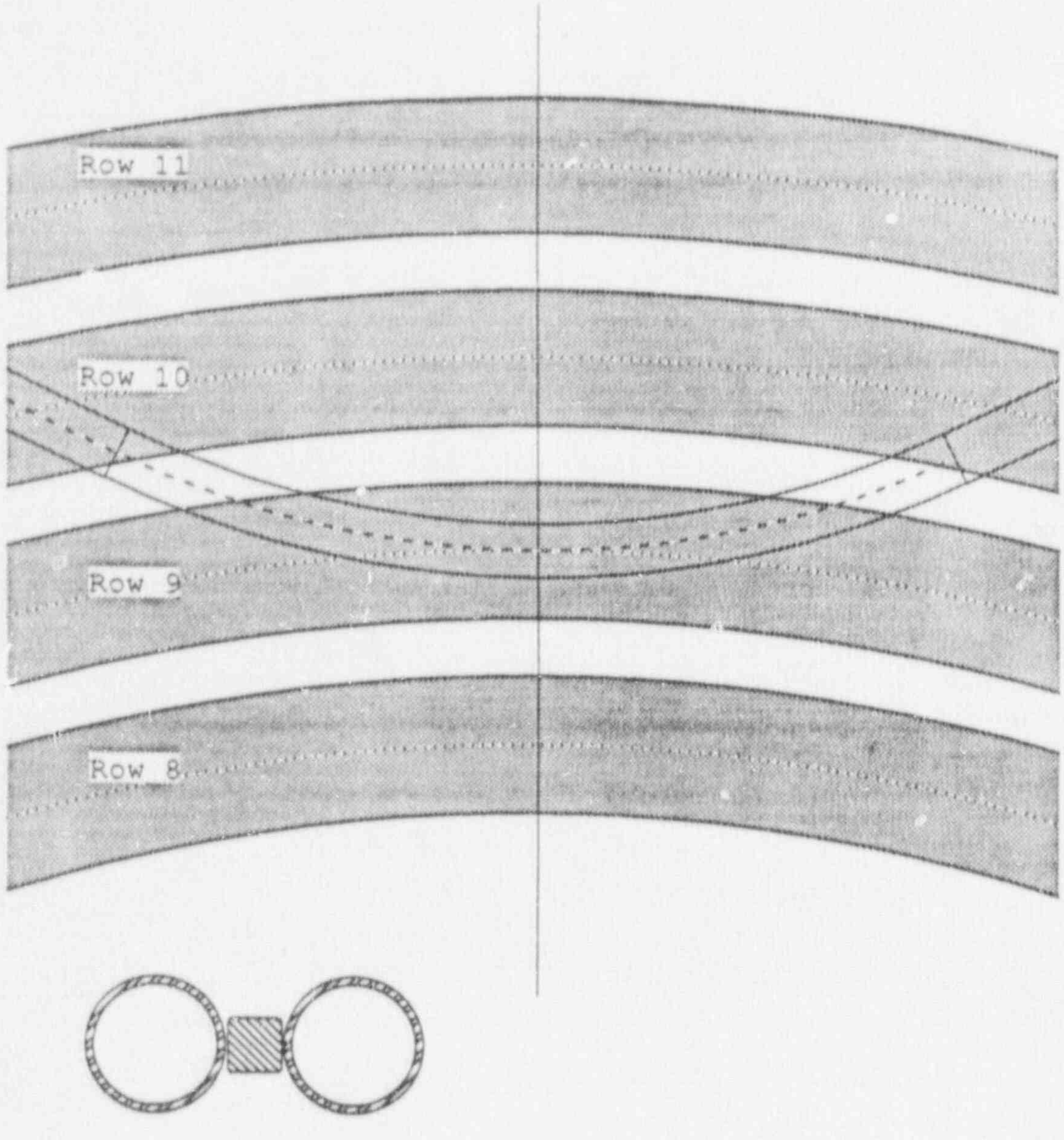

Figure 6-5 AVB Projection Depth = 9.00

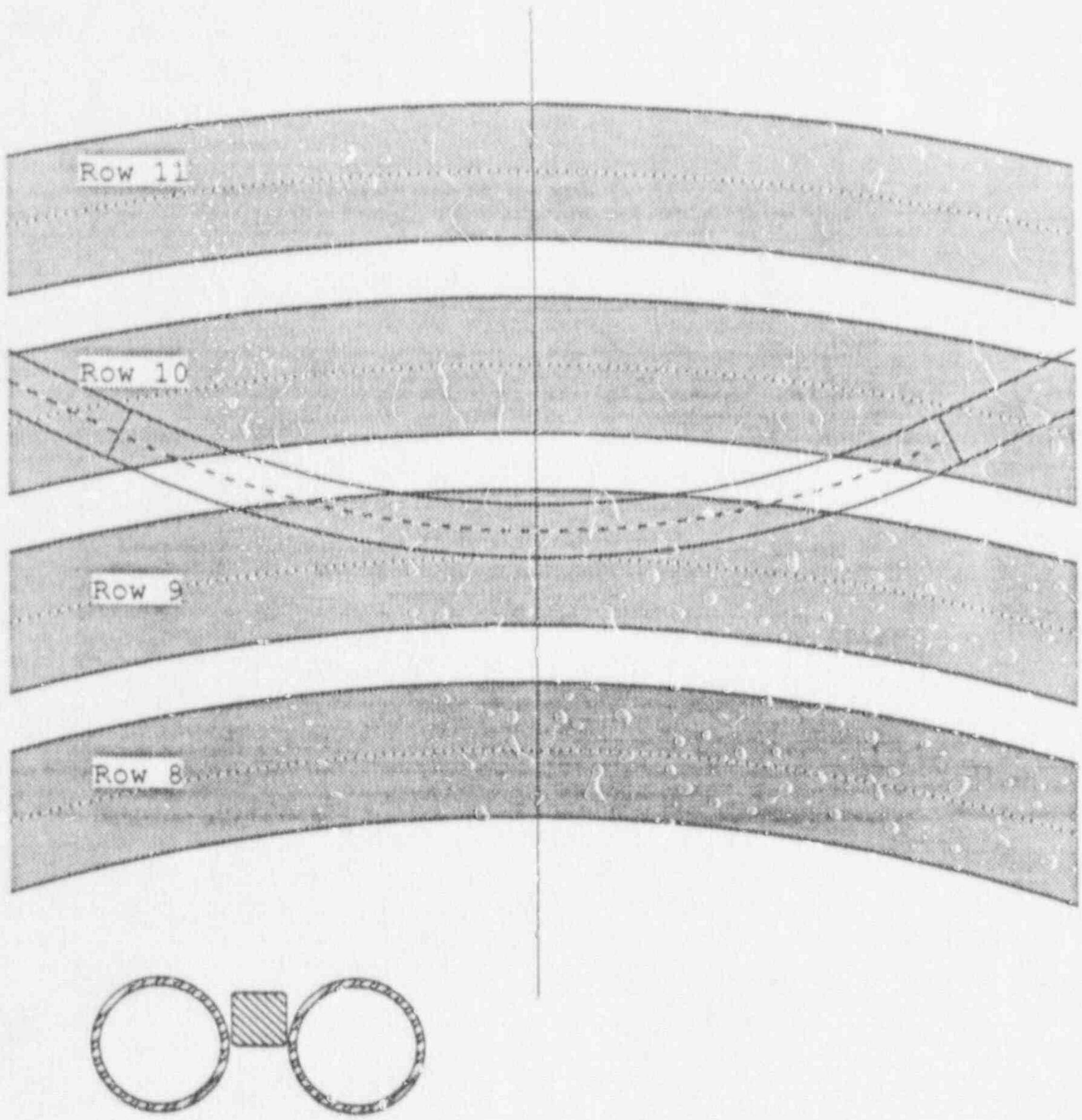

NTS

Figure 6-6 AVB Projection Depth = 9.15

7.0 THERMAL AND HYDRAULIC ANALYSIS

This section presents the results of a thermal and hydraulic analysis of the flow field on the secondary side of the steam generator using the 3-D ATHOS computer code, Reference (7-1). The major results of the analysis are the water/steam velocity components, density, void fraction, and the primary and secondary fluid and tube wall temperatures. The distributions of the tube gap velocity and density along a given tube were obtained by reducing the ATHOS results. The bundle parameter distributions used in the V. C. Summer analysis are based on ATHOS results for another Model D3 steam generator (which will be referred to as the Reference Model) having similar operating conditions. The effect of small differences in operating conditions between the V. C. Summer generators and the other D3 generator were accounted for by applying an adjustment factor to the computed stability ratios.

In the following subsections, operating data for V. C. Summer are presented along with a comparison to corresponding conditions of the Reference Model D3. As part of this comparison, a one-dimensional relative stability ratio calculation is described. The stability ratios for V. C. Summer are adjusted in this manner. A description of the Reference D3 ATHOS model and sample results are included in the next two sections. Section 7.4 describes an analysis of the operating history data for V. C. Summer. The final section discusses the effect of future operation at differing full power steam pressures.

7.1 V. C. Summer Steam Generator Operating Conditions and 1D Relative Stability Ratio Analysis

Recent steam generator operating condition data for the V. C. Summer unit were provided by SCE&G. The data are representative of full power operation during the most recently completed fuel cycle, Cycle 5. Table 7-1 provides the data for only the most limiting of the three steam generators, SG-C.

With these data, calculations were completed using the Westinghouse SG performance computer code, GEND3, to verify the plant data and to establish a complete list of operating conditions required for the ATHOS analysis. The

GEND3 code determines the primary side temperatures and steam flow rate required to obtain the specified steam pressure at the given power rating. Besides confirming these parameters, the code calculates the circulation ratio which is of primary importance to the stability ratio analysis since it, together with the steam flow establishes the total bundle flow rate and average loading on the tubes. It also provides an overall indication of the voids within the tube bundle since the bundle exit quality is inversely proportional to the circ ratio (X_{exit} = 1/circ ratio). The calculated circulation ratio is also listed in Table 7-1. In addition, the operating conditions on which the Reference Model D3 ATHOS study was based are listed.

With respect to their effect on tube stability ratios, three of the operating parameters listed in Table 7-1 are of prime importance: [

]^{a,c}

An overall measure of the effect of different operating conditions on the stability ratio can be obtained from a parameter termed the 1D relative fluidelastic stability ratio. This ratio compares the fluidelastic stability ratio computed for a particular set of operating conditions to a reference stability ratio. For the V. C. Summer analysis, the relative stability ratio technique is used to define an adjustment factor which is applied to the Reference Model D3 stability ratios to account for the differences in operating conditions. The same technique is used to evaluate the effect of past operation on the stability ratio (Section 7.4) and the effect of future operation with reduced steam pressure/increased tube plugging (Section 7.5).

The fluidelastic stability ratio is defined as the ratio of the effective fluid velocity acting on a given tube to the critical velocity at which large amplitude fluidelastic vibration initiates:

$$\text{Fluidelastic Stability Ratio, SR} = \frac{U_{effective}}{U_{critical\ at\ onset\ of\ instability}} \quad [1]$$

In this ratio, the effective velocity depends on the distribution of flow velocity and fluid density, and on the mode shape of vibration. The critical velocity is based on experimental data and has been shown to be dependent upon the tube natural frequency, damping, the geometry of the tube, the tube pattern, and the fluid density, along with the appropriate correlation coefficients.

The detailed calculation of this ratio using velocity and density distributions, etc., requires three-dimensional thermal/hydraulic and tube vibration calculations which are lengthy. Therefore, a simplified, one-dimensional version of this ratio has been used to provide a relative assessment technique for determining the effect of changes in operating conditions on the stability ratio. The relative stability ratio is defined by the following equation:

$$\left[\qquad \right]^{a,c} \quad [2]$$

In this equation "SUM" refers to V. C. Summer and "REF" to the Reference Model D3 operating condition. While this simplified approach cannot account for three-dimensional tube bundle effects, it does consider the major operational parameters affecting the stability ratio. Four components make up this ratio: a loading term based on the dynamic pressure (ρV^2), a tube incremental mass (m) term, the natural frequency of the tube (f_n), and a damping ratio (δ) term. It should be noted that the ratio is relative, in that each component is expressed as a ratio of the value for a given operating condition to that of a reference operating point.

[

]^{a,c}.

The particular damping correlation which is used for all normalized stability ratio calculations is based on a dented condition at the top tube support plate (a clamped condition, as discussed in Section 5.2). The clamped condition is also assumed in calculating the tube natural frequency.

As shown at the bottom of Table 7-1, the effect of the difference in operating conditions results in a [ ]^{a,c} decrease in relative stability ratio for V. C. Summer compared to the Reference Model D3. The higher pressure for V. C. Summer [ ]^{a,c} is the primary factor leading to this decrease. The stability ratios for the Reference Model D3 steam generator are thus adjusted by a [ ]^{a,c} multiplier to generate a set of 3D stability ratios for V. C. Summer.

Justification for use of a one-dimensional relative stability ratio adjustment factor is [

]^{a,c}

7.2 ATHOS Analysis Model

The calculation of relative stability ratios involves comparing the stability ratio calculated for one or more tubes in a given plant to the ratio calculated for the ruptured Row 9 Column 51 tube in the North Anna Series 51 steam generator. It makes use of ATHOS computed flow profiles for both tube bundles. Since the presence of AVBs in the U-bend region of a tube bundle could influence the overall flow field and/or the local flow parameters for a particular tube of interest, some discussion of the treatment of AVBs is necessary before presenting a description of the ATHOS model.

The ATHOS code does not include the capability to model the presence of the AVBs in the U-bend region. However, Westinghouse has modified the code to include the capability to model the AVBs via flow cell boundary resistance factors. Practical lower limits of cell size in the ATHOS code, however, prevent a fine grid representation of the AVB V-bar shape which, in turn, limits the accuracy of the AVB representation. ATHOS calculations have been performed with and without AVBs in the model. [

]a,c

The Reference Model D3 analysis is based on a Cartesian coordinate system for the array of flow cells instead of the typical, and more widely used, cylindrical coordinate system. With a Cartesian coordinate system the tube array and any AVBs are arranged in a square pitched configuration which is in-line with the coordinate axes. This alignment provides an improved representation of the tube region of interest in the bundle.

The ATHOS Cartesian coordinate system model for the Reference Model D? steam generator consists of 18,720 flow cells having 30 divisions in the x-axis (perpendicular to the tubelane) direction, 16 divisions in the y-axis (along the tubelane) direction and 39 divisions in the axial (z-axis) direction. In the ATHOS analysis, the steam generator is considered to be symmetrical about the x-axis of the tube bundle. The model therefore, consists of one-half of the hot leg and one-half of the cold leg sides of the steam generator. Figures 7-1 and 7-2 show the plan and the elevation views of the model. These two figures show the layout of the flow cells and identify locations for some of the geometric features.

As shown in Figure 7-1, with the Cartesian coordinate system, the circular wrapper boundary is represented by a step-wise wall as indicated by the heavy lines. All of the flow cells outside the simulated wrapper boundary above the first axial slab were blocked off by specifying extremely high flow resistances on the faces of the appropriate cells. Tubelane flow slots in the tube support plates are modeled also.

Figure 7-2 shows the elevation view of the model on the vertical plane of symmetry of the steam generator. The feedwater nozzle is located at axial indices IZ=11 and 12. Ten axial layers of cells were included in the U-bend near the top tube support (Figure 7-2, IZ=27 to IZ=36) to more closely model the flow conditions in the area of interest.

Figure 7-3 reproduces the plan view of the model but with the tube layout arrangement superimposed. This figure illustrates the locations of the tubes in the various flow cells. The grid lines in the Cartesian model are in-line with the tube array, providing for all of the tubes to be within the boundary of the flow cells. The fineness of the cell mesh is evident; the largest cells contain only 25 tubes while some of the smallest cells include only three tubes. Note, in particular, that additional detail was added near the bundle periphery (IY=13-16) to more closely model the inner radius tubes.

7.3 ATHOS Results

The results from the ATHOS analysis consist of the thermal-hydraulic flow parameters necessary to describe the 3-D flow field on the secondary side of the steam generator (velocity, density, and void fraction) plus the distributions of the primary fluid and mean tube wall temperatures. The secondary side mixture velocity is composed of three components (Vx, Vy, and Vz) which ATHOS computes on the surfaces of the flow cell. Since the local gap velocity surrounding a tube is required in the vibration analysis, a post-processor is used which: a) interpolates among the velocity components for the cells located nearest to the tube of interest and, b) accounts for the minimum flow area between tubes to calculate the tube-to-tube gap velocity. The post-processor performs the necessary interpolations to determine both in-plane and out-of-plane gap velocities at specific intervals along the length of a tube. It also interpolates on the ATHOS cell-centered density and void fraction to determine the required local parameters along the tube length. The output of the post-processing is a data file which contains these parameter distributions for all the tubes in the generator and which provides a portion of the input data required for tube vibration analyses.

Figure 7-4 shows a vector plot of the flow pattern on the vertical plane of symmetry of the steam generator (the vectors are located at the center of the flow cells shown in Figure 7-2). The zig-zag flow pattern through the split flow preheater is clearly shown in the figure. On the hot leg side the vertical flow upward through the half-moon cut-out at the center of flow distribution Plate A is also clearly shown. The vertical velocity (V_Z) component entering the U-bend region on the hot leg side is about twice that of the cold leg side as seen in Figure 7-5 (at model vertical layer index IZ=27). The figure also shows the high V_Z-component of the flow leaving the three flow slots on the top tube support plate (PLATE T) at the middle of the figure. The lateral velocity components, $VR = (Vx^2 + Vy^2)^{1/2}$ on the same horizontal plane (IZ=27) are shown in Figure 7-6. Viewing Figures 7-5 and 7-6 it is seen that at the entrance to the U-bend region the vertical velocity component is about twice that of the lateral velocity resultant on the hot leg side, whereas the resultant lateral velocity on the hot leg side is several times greater than that on the cold leg side. Figure 7-7 shows the plot of the void fraction contours on the vertical plane of symmetry of the steam generator. In the preheater the void fraction is essentially zero. By comparison, the hot leg side void fraction develops rapidly from the lower bundle region. In the U-bend region the void fraction is above 0.95 on the hot leg side, decreasing to about 0.70 at the bundle periphery on the cold leg side.

Figures 7-8, 7-9 and 7-10 show a sample of the individual tube gap velocity and density distributions along three tubes at Row 10. In each figure the gap velocity and density along the length of the tube are plotted from the hot leg tubesheet end on the left of the figure to the cold leg end on the right. The mixture gap velocity and density distributions are required as part of the input for tube vibration analysis to determine the tube stability ratios. These data were generated by the ATHOS post-processor for each tube in the model and stored in a data file. The data file was then utilized in the subsequent stability ratio calculations. Figure 7-11 shows the plot of the average in-plane gap velocity normal to the tube and density profiles as a function of the column number along Row 10. The average values were taken as the numerical average of the parameter over the entire 180° span of a U-bend at a given column location. The average velocity values are between 10.0 and 11.0 ft/sec. The velocity variations seen in the figure between Columns 35 and 55 are related to the effects of the flow slots along the tubelane of the top tube support plate.

7.4 Relative Stability Ratio Over Operating History

One aspect of the evaluation of the V. C. Summer steam generators is to examine the operating history data and use it to determine the susceptibility to fatigue from fluidelastic vibration resulting from the 7-1/2 years of operation. This assessment has been completed through the use of the relative stability ratio technique described previously in Section 7.1. In this application a normalized stability ratio is defined which compares the fluidelastic stability ratio for each period of a plant's operation (fuel cycle) to a reference stability ratio based on a recent operating condition.

A plot of this ratio against operating time, therefore, provides a relative indication of the effect of past operation on the plant's fluidelastic stability ratio. This normalized time-dependent ratio is subsequently combined with an absolute stability ratio for the reference operating point derived from detailed three-dimensional thermal/hydraulic and tube vibration calculations. [

]a,c

As discussed previously in Section 7.1, the reference three-dimensional stability ratio calculations for the V. C. Summer steam generators were based on Reference Model D3 ATHOS study results along with an adjustment to account for the difference in operating conditions between V. C. Summer and the reference plant. In addition to the reference stability ratios for the recent operating conditions, a series of calculations were completed to generate a normalized stability ratio for each of the five fuel cycles since V. C. Summer became operational in October, 1982. Data for this evaluation are summarized in Table 7-2. Included are typical values for full load steam pressure and primary fluid average temperature in each cycle. The number of days that the plant has operated within three power intervals (36-60%, 61-95%, and 96-100%) are also listed. [

]a,c

The resulting normalized stability ratios are shown in Figure 7-12. In this figure, the normalized stability ratio is plotted against cumulative operating time above 61% power. The reference value (=1.00) is based on the recent operating condition. The results indicate that, as a result of the general decrease in steam pressure which has occurred, the relative stability ratio has increased about [ ]a,c from Cycle 1 to the current cycle. Note that the calculations for Cycle 5 were projected forward from 11/27/89 to 3/16/90.

7.5 Effect of Steam Pressure on Relative Stability Ratio

Typically, future fatigue usage is computed assuming continued operation through the end of the 40 year design basis with the current reference operating conditions and relative stability ratios (RSRs). In addition to this calculation, the effects of future long-term increases in tube plugging have been evaluated. Plugging has an adverse effect on the fatigue usage because it results in lower steam pressures. Reduced pressure leads to higher U-bend velocities for the same flow rate and reduced damping. Both of these factors result in higher RSRs.

During the most recent fuel cycle, the average plugging level among the three generators was 7.8%. SCE&G estimated that the plugging for Cycle 6 may average 11%. Based on levels selected by SCE&G, two future plugging scenarios have been examined. In the first, it was assumed that at the next startup, 12% plugging is present and that this condition exists through 3/93, at which time the plugging increases to 15% for operation through 3/96. In the second scenario, the plugging is assumed to be 15% at the next startup and is maintained at this level for the six years of operation, through 3/96.

Based on average tube plugging, GEND performance calculations predict that the steam generator exit pressure will change from the current 941 psia to 926 psia for 12% plugging and to 911 psia for 15% plugging. These calculations are based on the assumption that the current 587°F T_{avg} will be maintained, and indicate that the relative stability ratio will increase by [ ]^{a,c} for the SG exit pressures calculated for 12% plugging and by [ ]^{a,c} for 15% plugging. These results have been included in Figure 7-12. Note that the pressure calculated for the assumed 15% plugging (911 psia) is close to the valves wide open pressure (915 psia) below which full power cannot be maintained without turbine modifications. Therefore, the [ ]^{a,c} RSR multiplier represents a reasonable bounding value for future operation assuming full power operation.

Although these calculations were based on specific levels of tube plugging, [

]^{a,c}

References:

7-1 L. W. Keeton, A. K. Singhal, et al. "ATHOS3: A Computer Program for Thermal-Hydraulic Analysis of Steam Generators", Vols. 1, 2, and 3, EPRI NP-4604-CCM, July, 1986.

Table 7-1

V. C. Summer Steam Generator Operating Conditions and Comparison with Reference Model D3 ATHOS Analysis

	V. C. Summer (SG-C)	Reference Model D3	
			a,c
Thermal Power (MWt)	950		
Steam Flow Rate (lbm/hr)	4.13×10^6		
Feedwater Inlet Temperature (°F)	432		
Steam Pressure (psia)	941		
Water Level (% of span)	63.6		
Primary Inlet/Outlet Temperatures (°F)	618/556		
Calculated Parameters			
			a,c
Circulation Ratio			
Bundle Flow Rate (lbm/hr)			
1D Relative Stability Ratio (Normalized to Reference Model D3)			

Table 7-2
V. C. Summer Operating History Data

Cycle	Beginning	End	Distribution of Days in Each Power Interval 96-100%	61-95%	36-60%	Full Load Values: Steam Pressure* (Psia)	Primary Avg. Temp.* (Deg F)	Feedwater Temperature* (Deg F)	Calculated Steam Flow* (lbm/hr)	Calculated Circ Ratio*
1	22-Oct-82	28-Sep-84	275	101	101	964	587	435		
2	18-Dec-84	05-Oct-85	211	32	8	960	587	435		
3	14-Dec-85	06-Mar-87	368	44	10	958	587	434		
4	06-Jun-87	16-Sep-88	406	15	9	948	587	433		
5	26-Dec-88	16-Mar-90**	309	18	23	941	587	432		
			1569	210	151					

a,c

Notes:

* Basis: most limiting generator, SG-C.
** Projected end of cycle 5, last data on 11/27/89. All projected operation assumed to be at full power.

a,c

Figure 7-1 Plan View of ATHOS Cartesian Model for Reference Model D3

a,c

Figure 7-2 Elevation View of ATHOS Cartesian Model for Reference Model D3

a,c

Figure 7-3 Plan View of ATHOS Cartesian Model for Reference Model D3 Indicating Tube Layout

a,c

Figure 7-4 Flow Pattern on Vertical Plane of Symmetry

a,c

Figure 7-5 Vertical Velocity Contours on a Horizontal Plane at the Entrance to the U-Bend Region (IZ=27)

a,c

Figure 7-6 Lateral Flow Pattern on Horizontal Plane, at the Entrance to the U-Bend Region (IZ=27)

a,c

Figure 7-7 Void Fraction Contours on Vertical Plane of Symmetry

a,c

Figure 7-8 Tube Gap Velocity and Density Distributions for Tube Row 10/Column 38

a,c

Figure 7-9 Tube Gap Velocity and Density Distributions
for Tube Row 10/Column 45

a,c

Figure 7-10 Tube Gap Velocity and Density Distributions for Tube Row 10/Column 50

a,c

Figure 7-11 Average Velocity and Density in the Plane of the U-Bends Normal to Row 10

a,c

Figure 7-12 V. C. Summer Normalized Stability Ratio Based on High Power (>61%) Operation

8.0 PEAKING FACTOR EVALUATION

This section describes the overall peaking factor evaluation to define the test based peaking factors for use in the tube fatigue evaluation. The evaluation of the eddy current data to define the AVB configuration for North Anna 1 Tube R9C51 is described. This configuration is critical to the tube fatigue assessments as the peaking factors for all other tubes are utilized relative to the R9C51 peaking factor. Uncertainties associated with applying the air model test results to the tube fatigue assessments are also included in this section. Included in the uncertainty evaluation are the following contributions:

- Extrapolation of air test results to two phase steam-water
- Cantilever tube simulation of U-bend tubes
- Test measurements and repeatability
- AVB insertion depth uncertainty

8.1 North Anna 1 Configuration

8.1.1 Background

The AVB configuration of the ruptured tube in North Anna, R9C51, is the reference case for the tube fatigue evaluations for other plants. In accordance with the NRC Bulletin 88-02, the acceptability of unsupported tubes in steam generators at other plants is based on tube specific analysis relative to the North Anna R9C51 tube, including the relative flow peaking factors. Thus, the support conditions of the R9C51 tube are fundamental to the analyses of other tubes. Because of the importance of the North Anna tube, the support conditions of this tube, which were originally based on "AVB Visible" interpretations of the eddy current test (ECT) data (Figure 8-1), were re-evaluated using the projection technique developed since the North Anna event. The projection technique is particularly valuable for establishing AVB positions when deposits on the tubes tend to mask AVB signals such as found for the North Anna 1 tubes. The results of this evaluation are summarized below.

8.1.2 Description of the Method

The basic method utilized was the projection technique in which the AVB position is determined based on measured AVB locations in larger row tubes in the same column. In this study, the projection technique was utilized in the "blind" mode, (AVBs called strictly based on the data) as well as the reverse mode (data examined on the basis of predicted AVB positions). The objective of this application was, with the greatest confidence possible, to establish the positions of the AVBs in an 8 column range around the R9C51 tube in North Anna 1, Steam Generator C.

8.1.3 Data Interpretation

The ECT traces for the U-bends in Rows 8-12 (in one case, 13) were examined for Columns 48-55. The original AVB visible calls are shown in Figure 8-1. The data were examined by an eddy current analyst experienced in reading these traces, and by a design engineer knowledgeable in the geometry of the Model 51 U-bend region.

The intent of this review was to determine if the presence or absence of AVBs as shown in Figure 8-1 could be confirmed using the AVB projection technique. Preliminary projected AVB positions were based on geometric data provided for a few of the tubes near R9C51. The features which were sought were evidence of data "spikes" where AVBs were predicted, offset indications (multiple spikes) where offset AVBs were predicted, single indications where single AVB intersections were predicted, etc. The data evaluation method used was a critical examination of the data, which was biased toward the presence of AVBs unless a confident call of "no AVB" could be made, and then checking the consistency of the data among the tubes in a column and against the theoretical data for the predicted AVB positions. [

]^{a,c}.

Figure 8-4 is the "AVB visible" map for columns 48 through 55, based on the critical review of the data. It should be noted that the original data interpretations and the review interpretations are consistent.

8.1.4 Projections

The [ ]^{a,c} ECT traces were utilized for projecting the position of the AVBs according to the standard format of the projection method.

The results of the projections are presented in Figure 8-5, which shows a matrix of projections for tube rows 8 through 13 in columns 48 through 55. For many of the tubes, more than one, and as many as three, projection values are shown. Multiple projections are expected for a tube if the AVBs on either side of the tube are not at the same elevation, or if the upper and lower AVB support that tube. As many as four different projections are possible if it is assumed that the tube is supported by the upper and lower AVBs, and both upper and lower bars are staggered in elevation as shown in Figure 8-2.

The logic in arranging the projection data is based on the following two rules:

Rule 1. The projections of the same AVB based on different tubes in the same column [ ]^{a,c}.

[

]^{a,c}.

Rule 2. Two adjacent tubes in the same row [ ]^{a,c}. Consequently, the difference in the [ ]^{a,c}.

The implementation of this is that if the position (either left or right) of a projected AVB is assumed for a column, then the projections in the adjacent columns are also [

$]^{a,c}$.

The arrangement of the AVBs as shown in Figure 8-5 satisfies the rules above and is consistent with the rupture of R9C51. The resulting AVB arrangements, based on the projection matrix of Figure 8-5 is shown in Figure 8-6.

8.1.5 Conclusions

The general AVB arrangement surrounding the ruptured tube in North Anna-1, Steam Generator C, which was the basis for the analysis, is confirmed by a detailed critical review of the ECT data. Differences exist in the AVB pattern between tube columns 48-49, in which the AVBs appear to be less inserted than previously indicated. The pattern of Figure 8-6 is the best fit to the rules which were adopted for determining the position of the AVBs, as well as consistent with explanation of the tube failure.

The basis of the review was a projection technique which utilizes data from tubes one or more rows removed from the actual inserted position of the AVB to determine the position of the AVB. The intent of the review was to establish the positions of the AVBs by confirming or eliminating features of AVB alignments such as side to side offsets, etc. of the AVBs adjacent to the tubes. Overall, the conclusions regarding the positions of the AVBs around R9C51 in North Anna-1, Steam Generator C are based on consistency among all the available data.

8.2 Test Measurement Uncertainties

The descriptions of the peaking factor tests and apparatus were provided in Section 5.4. All practical measures were taken to reduce uncertainties. Nevertheless, some still remain and should be properly accounted for. The important parameter measured during testing that has a significant impact on peaking factor is the air velocity. The air velocity at test section inlet was measured using a [ ]^{a,c}. Based on considerable experience with the use of such instruments, it is known that the magnitude of uncertainty is very small. A [ ]^{a,c} measurement uncertainty is used in this analysis based on past experience.

8.3 Test Repeatability

During the peaking factor testing of AVB configuration, each test was performed at least two times to confirm repeatability. It has been demonstrated that the tests are quite repeatable with the results often falling within 2 or 3% of one another for the repeat tests. An upper bound value of 5% was used in the current uncertainty analysis.

8.4 Cantilever vs U-Tube

A first order estimate can be made of the validity of modeling a U-bend tube by a cantilever tube in tests to determine the effects of AVB insertion depth on the initiation of fluidelastic vibration. The following assumptions are used:

a,c

[ ]

a,c

[

]

For the purposes of this estimate, the geometry of the cantilever measuring tube in the air test model is compared with the geometry of a prototypical Row 10 tube. [

]a,c.

The comparison between a U-bend tube and the model tube involve the consideration of an effective velocity associated with the flow perturbation caused by the AVBs. [

]a,c

[

]^{a,c}. Using these values, the ratio of the effective velocity for the cantilever measuring tube to that for the U-bend tube is about [ ]^{a,c} for the case treated.

A similar evaluation can be made for a Row 10 tube that lies in the projection or shadow of an AVB that is inserted to a depth required to support a Row 9 tube. [

]^{a,c}.

The net result is that the ratio of the effective velocity for the cantilever tube to that for the U-bend tube is about [ ]^{a,c}.

These results indicate that, for the particular assumptions used, the cantilever tube model appears to be a reasonable representation of the U-bend with respect to determining relative peaking factors for different AVB configurations. This evaluation also shows that, on the average, the magnitude of the systematic uncertainty associated with the use of cantilever tube to simulate the U-bend is about [ ]^{a,c}.

8.5 Air vs Steam-Water Mixture

The local peaking factors from the air tests can be applied to the steam generator steam/water conditions either as a direct factor on the mixture velocity and thus a direct factor on a stability ratio, or as a factor on the steam velocity only with associated impacts on density, void fraction and damping. This method leads to a reduction in tube damping which enhances the peaking factor compared to the direct air test value. For estimating an absolute stability ratio, this application of the peaking factor is a best estimate approach. However, for the evaluation of tubes relative to stability ratio criteria, it is more conservative to minimize the peaking factor for the North Anna Unit 1 tube R9C51 through direct application of the air test peaking factor. This conservative approach is therefore used for evaluating tube acceptability.

Under uniform AVB insertion (or aligned AVB insertion) there are no local open channels for flow to escape preferentially. Therefore, air flow is approximately the same as steam/water flow relative to velocity perturbations. Under non-uniform AVB insertion the steam/water flow may differ from air, as the steam and water may separate from each other when an obstruction, such as an AVB, appears downstream. The water would continue along the same channel while steam readily seeks a low resistance passage and thus turns into adjacent open channels. Two phase tests indicate a tendency for steam to preferentially follow the low pressure drop path compared to the water phase.

Based on the above discussion, the F_i are considered to more appropriately apply to the steam phase. Thus, it follows that mixture mass velocity for the tube subject to flow perturbation can be written as follows:

[ ] a,c

where D_g is the vapor density, D_f the water density, F_a the velocity peaking factor determined from air tests, j_g* the nominal superficial vapor velocity, and j_f* the superficial water velocity. Steam quality can then be determined as follows:

$$\left[\qquad \right]^{a,c}$$

The Lellouche-Zolotar correlation (algebraic slip model), as used in the ATHOS code, is applied to determine void fraction. Subsequently, mixture density, velocity and damping coefficients for the tube which is not supported and subject to flow perturbation is evaluated. Therefore, similar to the air velocity peaking factor, local scaling factors of mixture density and velocity and damping coefficient can be readily determined. Finally, a local stability peaking factor for fluidelastic vibration can be calculated as follows:

$$\left[\qquad \right]^{a,c}$$

where Fs is the stability peaking factor, F_d the density scaling factor, F_v the velocity scaling factor, and F_{dp} the damping coefficient scaling factor. If we use the air velocity peaking factor without translating to steam/water conditions, then

$$\left[\qquad \right]^{a,c}$$

As shown in Table 8-1 stability peaking factors for the steam/water mixture are slightly higher than air velocity peaking factors. The difference between the steam/water and air peaking factors increases as the air peaking factor increases.

For application to tube fatigue evaluations, the ratio of the peaking factor for a specific tube to that for North Anna R9C51 is the quantity of interest. Larger values for this ratio are conservative for the tube fatigue assessment. The North Anna R9C51 peaking factor is one of the highest peaking factors. As discussed in Section 8.7, a peaking factor of nearly [$]^{a,c}$ is determined for the R9C51 tube. The differences between [

$]^{a,c}$. Typical values are shown in Table 8-2. These results show that the direct application of the air test data yields the higher relative peaking factor compared to R9C51. To obtain conservatism in the peaking factor evaluation, [

]^{a,c}.

Comparing the values in the first and last columns of Table 8-1, it may be noted that the stability peaking factor for steam water is [ ]^{a,c} higher than the air velocity peaking factor. On the average, the uncertainty associated with the conservative use of air velocity peaking factor is [ ]^{a,c}.

The conclusion that peaking factor for steam/water flow would be higher due to the dependency of damping ratio on void fraction was supported by an alternate study. In this study, a section of steam generator tubes were simulated using the ATHOS code under prototypic flow conditions. The objective of this study was to examine the magnitude of the changes in void fraction and thus stability ratio as a consequence of non-uniform AVB insertion patterns. The current version of ATHOS has modeling limitations that prevent accurate modeling of local geometry effects. In addition, it is believed that an analysis using two-fluid modeling procedure is mandatory to a calculation of the peaking factors for a steam generator to account for the preferential steam flow along the low resistance path. Consequently, the intent of this analysis is only to help bound the uncertainty on void fraction effects from extrapolating the air tests to steam-water.

First the analysis was conducted with uniformly inserted AVBs in the ATHOS model. The ATHOS results were processed by the FLOVIB code to determine stability ratios for the specific tubes of interest. The calculation was repeated using a non-uniform AVB insertion pattern in the model. The results show that the void fraction distribution changes as a result of flow perturbation. Further, the impact on stability ratio resulting from the changes in void fraction profiles was about [ ]^{a,c}. This alternate calculation provides independent corroboration of the prior discussion regarding the stability peaking factors under steam-water conditions vs in air.

8.6 AVB Insertion Depth Uncertainty

The most significant uncertainty for the low peaking configurations is not in the test results, but in the determination of actual AVB insertion patterns adjacent to specific tubes. The methodology used for obtaining the AVB insertion patterns from eddy current data can ascertain the AVB location only approximately. The effect on peaking factor resulting from this uncertainty is addressed using test results of AVB configurations that varied from one another by up to [$]^{a,c}$.

Based on maps of AVB insertion depth of various plants, several configurations have been tested for determining fluidelastic instability flow rate by an air cantilever model. Stability peaking factors were then determined from the ratio of critical flow rate for a uniform AVB insertion configuration to a specific configuration. Figure 8-7 summarizes the AVB configurations tested.

Position of AVB insertion depth is determined from Eddy Current Test (ECT) data. Positioning of AVB from ECT data reading is subject to uncertainty; its accuracy is probably about [$]^{a,c}$. A change of an AVB insertion depth in a given configuration leads to a different configuration, and thus a different peaking factor. A review of the tested AVB type has been made and results summarized in Table 8-3. As can be seen, a decrease in depth of an appropriate AVB tends to decrease the peaking factor, for instance, a [$]^{a,c}$. Such a trend can be explained; a decrease in a specific AVB depth will open up more channels for incoming fluid to distribute and thus less flow perturbation. However, this applies only to those changes without inducing the reinforcement of flow perturbation from upstream to downstream.

On the average, the uncertainty in peaking factor resulting from small variations in AVB insertion (of the order of 1/2 tube pitch) is found to be [$]^{a,c}$.

8.7 Overall Peaking Factor with Uncertainty

As discussed in the previous subsections, there are several aspects to be considered in applying the laboratory test data to steam generator conditions. These considerations were reviewed one at a time in those subsections. This section will integrate the pieces into one set of stability peaking factors.

Looking forward to how these peaking factors are used in the analysis (Section 9), the relative stability ratio calculated for a given tube without the consideration of flow peaking is corrected using the ratio of the peaking factor of the specific tube to that of the North Anna R9C51 tube (Configuration 1a).

It is to be noted that the test results would be applied as ratios of a specific tube peaking factor to the R9C51 peaking factor. This will reduce the influence of some uncertainties since the systematic uncertainties would affect both the numerator and the denominator in the ratio of peaking factors. The major difference will be in those configurations whose peaking factors are significantly lower than that of R9C51. The approach employed here is intended to provide that conservative peaking factors are employed for such apparently low peaking configurations.

The uniform AVB configuration (2a) is selected as a reference configuration, and the peaking factors of all configurations tested are recomputed on the basis of this reference. As discussed below, some of the test uncertainties are applied to the reference case to account for its significantly low peaking relative to the R9C51 configuration.

The uncertainties in the test results and their extrapolation are those due to test measurements, test repeatability, cantilever tubes in the test vs U-tubes in the steam generator, and air tests vs steam-water mixture. These were discussed in more detail in the previous subsections. The magnitude of these uncertainties are listed in Table 8-4.

Of these uncertainties, those due to measurement and repeatability of tests are random errors and can occur in any test. Therefore, these are treated together. The total random uncertainties are calculated by [ ]^{a,c}. The RSS value of these is [ ]^{a,c}. Since these can occur in any test, these are to be applied to all tests. One way of doing this is to apply it to the R9C51 value, that being in the denominator of the final peaking factor ratio. Thus the peaking factor for configuration 1a (R9C51) is reduced by this amount to yield a value of [ ]^{a,c} instead of the [ ]^{a,c} appearing in Table 5-2.

The next three uncertainties in Table 8-4 are systematic uncertainties. It could be argued that these appear in the peaking factors of both the specific tube under consideration and the R9C51 tube and are therefore counter balanced. However, the relative magnitude of these may be different, particularly for configurations with much lower peaking than R9C51. Therefore it was judged that the [ ]^{a,c}. Similarly, as noted above, the effect on peaking factor due to the uncertainty in the field AVB configuration is also included in this reference case. Thus, [ ]^{a,c}. The peaking factor of the reference configuration 2a (Table 8-5) is raised by this amount to a value of [ ]^{a,c}.

The change in peaking factors of configurations 1a and 2a resulting from the application of uncertainties as described above are shown in Column 3 of Table 8-5. The peaking factors of all configurations are recomputed on the basis of this reference configuration (2a). These values are displayed in Column 4 of Table 8-5.

Some of the uncertainties were applied to the reference configuration (2a) in order to apply them to all low peaking configurations conservatively. Thus, no configuration should have a lower peaking factor than this reference configuration. Therefore, when a peaking factor value less than [ ]^{a,c} is calculated for any configuration, (in Column 4 of Table 8-5), it should be altered to [ ]^{a,c}. Further, for some of the configurations that are conceptually similar, the more limiting (higher) value is used. For example, a peaking factor of [$]^{a,c}$ is used for configurations 5a and 5b based on their similarity to configuration 5c.

The final stability ratio peaking factors calculated on this basis (with configuration 2a as the reference) are shown in Table 8-6.

The overall conclusions from the peaking factor assessment are:

1. As noted in Table 8-4, five elements have been included in the uncertainty evaluation for the peaking factors. The uncertainty estimates were developed from both test and analysis results as described in Sections 8.2 to 8.6. The largest single uncertainty of [$]^{a,c}$ is attributable to uncertainties of up to [$]^{a,c}$ on determination of AVB insertion depths from field eddy current data. This relatively large uncertainty is applicable only to low peaking conditions where the AVB uncertainties can contribute to small peaking factors. The definition of "no flow peaking" was increased to encompass the small peaking effects from AVB insertion uncertainties. For the AVB patterns leading to significant peaking factors, AVBs were positioned within uncertainties to maximize the peaking factor. For these configurations, variations of AVB insertion within these uncertainties are expected to reduce the peaking factor compared to the final values of Table 8-6 and Figure 8-7.

2. Including uncertainties directed toward conservatively decreasing the peaking factor for the North Anna tube R9C51, the final R9C51 peaking factor is [$]^{a,c}$ relative to a no flow peaking condition such as with uniform AVB insertion depths.

8.8 Peaking Factors for Specific Tubes

Peaking factors for V. C. Summer were determined using the methodology described above. Table 8-7 summarizes the results of peaking factors. The AVB positions on each insertion pattern of Figure 8-7 should be carefully noted. Where the AVBs are shown [

]^{a,c}

In applying the methodology to V. C. Summer, maps of the AVB insertion depths shown in Figures 6-2 through 6-4 were first reviewed. The second step was to identify locations having significant AVB insertion configurations. In doing so, maximum allowable flow peaking factors were also reviewed column by column for Rows 8 through 13. Based on the V. C. Summer tube vibration analysis, flow peaking factors greater than [ ]^{a,c} for Row 8 and [ ]^{a,c} for Row 9 tubes would indicate the potential for tube fatigue.

After conservative estimates of peaking factors were made for specific tubes, those having peaking factors near the maximum allowable value were identified and AVB insertion depth was reviewed in the vicinity of the subject tube. If needed, the stability velocity, or the velocity at which unstable tube vibration initiates, was determined for the subject tube by testing the AVB insertion pattern in the Westinghouse Science and Technology Center Cantilever, Air Model. The peaking factor was then calculated using the stability velocity. For V. C. Summer, two supplementary configurations were tested. [

]^{a,c}

Determination of peaking factors for identified tubes shown in Table 8-7 are described in detail below. Sections 8.8.1 to 8.8.3 are divided into small tables for ease in following the description.

8.8.1 Steam Generator A

The following table gives the peaking factors for tubes with unique configurations of AVB insertion depths.

Steam Generator	Row No	Column No	Type of AVB Insertion Depth	Peaking Factor
A	8	22	[	] a,c
		11		
	9	83		
		71, 70		
		63		
		55		

For R8C22, type [ ]^{a,c} was selected and a peaking factor of [ ]^{a,c} resulted. Tube R8C11 belonged to type [ ]^{a,c} and thus a peaking factor of [ ]^{a,c} was obtained. Type [ ]^{a,c} was a good match for R9C83 and it then had a peaking factor of [ ]^{a,c}. Type [ ]^{a,c} was considered for tubes R9C71 and R9C70, and a peaking factor of [ ]^{a,c} was obtained. Both R9C63 and R9C55 had a peaking factor of [ ]^{a,c} for a selection of type [ ]^{a,c}.

8.8.2 Steam Generator B

Tubes with unique AVB configurations are listed together with their peaking factors.

Steam Generator	Row No	Column No	Type of AVB Insertion Depth	Peaking Factor
B	7	11	[	] a,c
	8	74		
		66		
	9	110		
		56		

Type [ ]^{a,c} was a conservative call for R7C11, R8C74, R8C66 and R9C110 and a peaking factor of [ ]^{a,c} resulted for all of them. R9C56 tube belonged to type [ ]^{a,c} and a peaking factor of [ ]^{a,c} was obtained.

8.8.3 Steam Generator C

The following table presents results of peaking factors.

Steam Generator	Row No	Column No	Type of AVB Insertion Depth	Peaking Factor
				a,c
C	7	88		
	8	98, 97		
		93		
	9	106		
		29		
		23		
		12, 11		
	10	106		
		23		
	12	5		
	13	5		

Type [ ]^{a,c} was selected for R7C88 and a peaking factor of [ ]^{a,c} resulted. Both R8C98 and R8C97 belonged to type [ ]^{a,c} and a peaking factor of [ ]^{a,c} was obtained.

Type [$]^{a,c}$ was selected for R8C93 and thus a conservative peaking factor of [$]^{a,c}$ resulted. Type [$]^{a,c}$ was considered for R9C106 and R9C29 and a peaking factor of [$]^{a,c}$ was obtained. Type [$]^{a,c}$ was selected for tube R9C23 and a peaking factor of [$]^{a,c}$ resulted. Type [$]^{a,c}$ was considered for both R9C12 and R9C11 and a peaking factor of [$]^{a,c}$ was obtained. Type [$]^{a,c}$ was used for R10C106 and a peaking factor of [$]^{a,c}$ resulted. Tube R10C23 belonged to type [$]^{a,c}$ which has a peaking factor of [$]^{a,c}$. Type [$]^{a,c}$ was selected for R12C5 and a peaking factor of [$]^{a,c}$ resulted. As for R13C5, it could be identified with type [$]^{a,c}$ and a peaking factor of [$]^{a,c}$ occurred.

Note that the bar between Columns 25 and 26 [

$]^{a,c}$ The same discussion applies to the tests configuration for R9C23, Configuration 8q.

All of the remaining SG-C tubes have no flow peaking, however, the fatigue and vibration analyses included several of the larger radius unsupported tubes without flow peaking, including R10C113, R10C11, R10C12, R10C2-8, and R11C4-8. (See Table 9-2.)

Table 8-1

Stability Peaking Factor Due to Local Velocity Perturbation

Scaling Factors for Steam/Water

Air Velocity Peaking Factor, F_a	Void Fraction Scaling, F_v	Density Scaling, F_d	Velocity Scaling, F_v	Damping Scaling, F_{dp}	Stability Peaking Factor, F_s

[ ]^{a,c}

NOTE: 1. Stability peaking factor for steam/water mixture is calculated as follows:

[ ]^{a,c}

2. Damping scaling factor is calculated using modal effective void fraction of [ ]^{a,c} for R9C51 tube.

Table 8-2

Comparison of Air and Steam-Water Peaking Factor Ratios

Air Peaking Factor	Air Peaking Ratio	Steam Peaking Factor	Steam Peaking Ratio

[ ] a,c

Table 8-3

Effect of Local Variation of AVB Insertion

Type A	Type B	A to B AVB Variation	Peaking Factor A	Peaking Factor B	Ratio (B/A)

a,c

a,c

Table 8-4

Uncertainties in Test Data and Extrapolation

	Source of Uncertainty	Type	Magnitude, %
			a,c
1.	Velocity measurement	Random	
2.	Test repeatability	Random	
3.	Cantilever vs U-tube	Systematic	
4.	Air vs steam-water mixture	Systematic	
5.	Field AVB configuration	*	

* This is not an uncertainty associated with the test data. It results from the inaccuracy in determining the true AVB position in the field using eddy current data.

Table 8-5

Extrapolation of Test Results to Steam Generator Conditions

Configuration	Test Data	Data with Uncertainties	Peaking Factor Referenced to Configuration 2a
			a,c
1a			
1b			
1k			
1w			
1x			
1y			
2a			
4a			
4b			
4c			
4d			
4o			
4x			
5a			
5b			
5c			
6a			
8p			
8q			

Table 8-6
Final Peaking Factors

Configuration	Peaking Factor [a,c]
1a	
1b	
1k	
1w	
1x	
1y	
2a	
4a	
4b	
4c	
4d	
4o	
4x	
5a	
5b	
5c	
6a	
8p	
8q	

Table 8-7
Stability Velocity Peaking Factors for Specific Tubes
V. C. Summer

Steam Generator	Row No	Column No	Type of AVB Insertion	Peaking Factor
				a,c
A	8	22		
		11		
	9	83		
		71, 70		
		63		
		55		
B	7	11		
	8	74		
		66		
	9	110		
		56		
C	7	88		
	8	98, 97		
		93		
	9	106		
		29		
		23		
		12, 11		
	10	106		
		23		
	12	5		
	13	5		

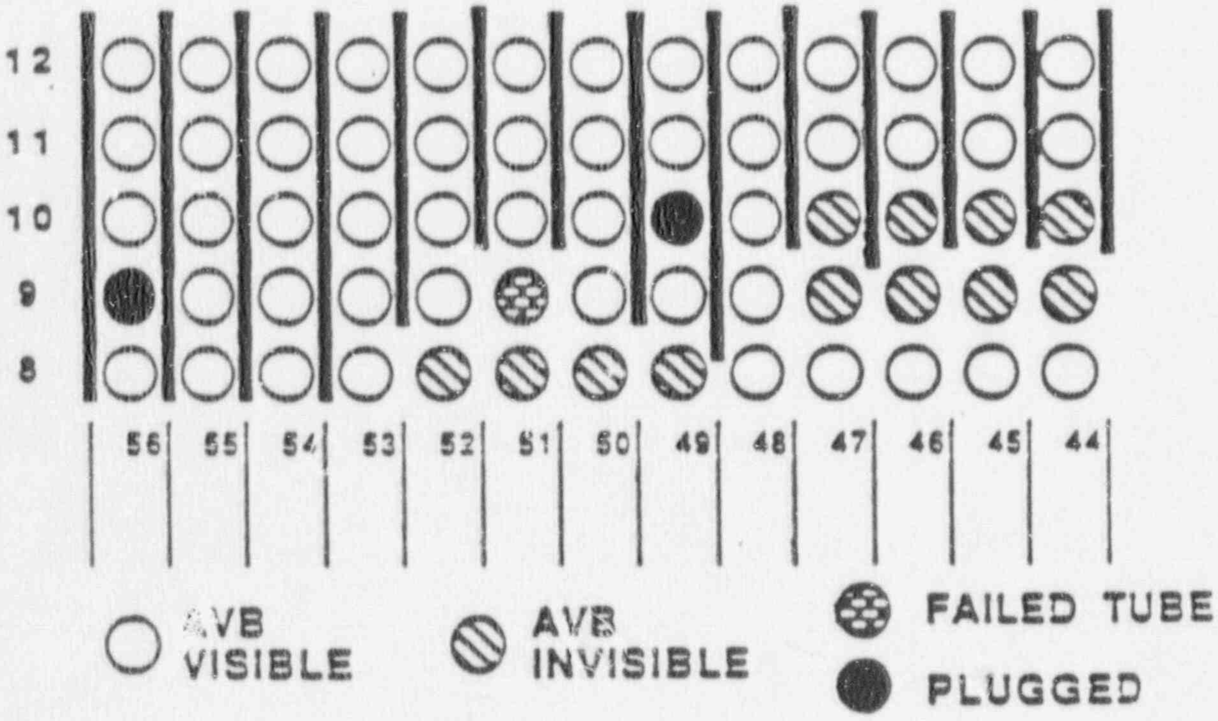

Figure 8-1 Original North Anna AVB Configuration (Configuration 1b)

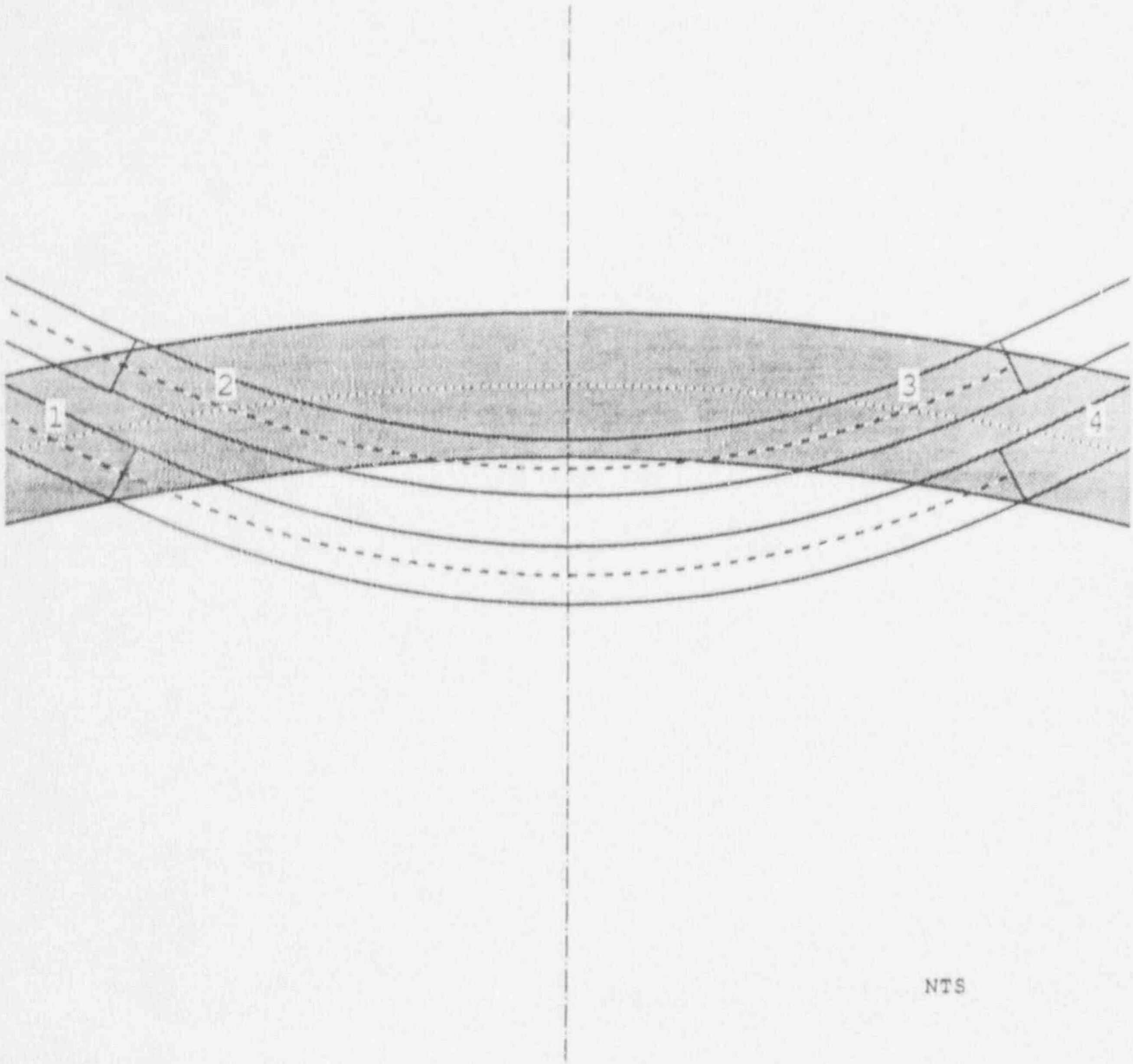

Figure 8-2

Schematic of Staggered AVBs

a,c

Figure 8-3 AVB "Pair" in ECT Trace

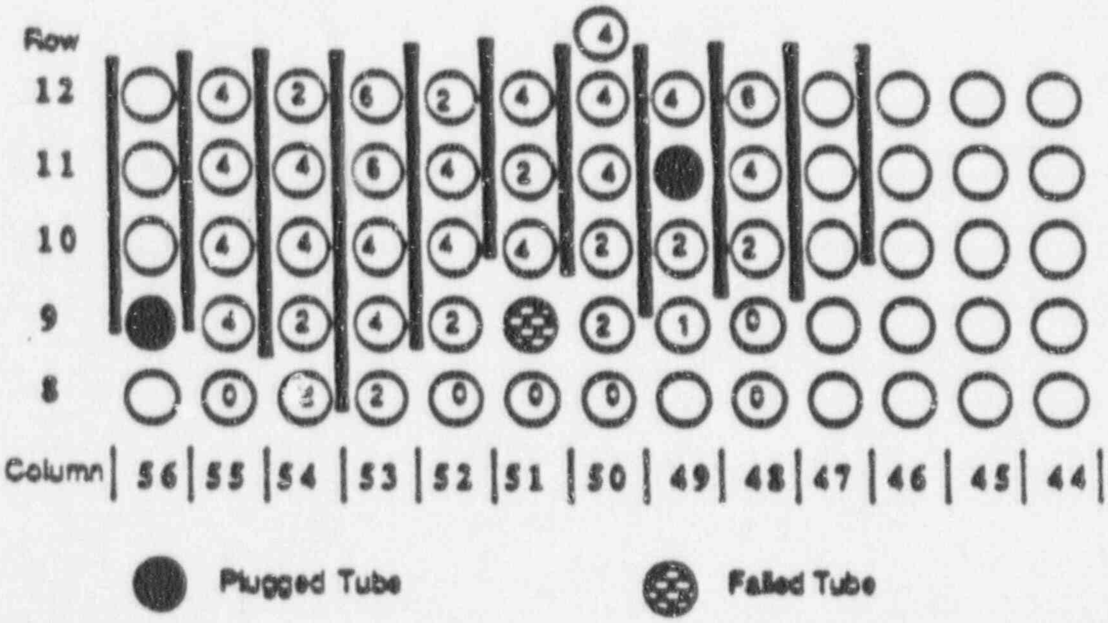

Numbers in circles in column range 48-55 represent readable AVB intersection signals, based on critical review of the ECT traces.. Open circle in this range means no data is available.

Figure 8-4 North Anna 1, Steam Generator C, AVB Positions
Critical Review "AVB Visible" Calls

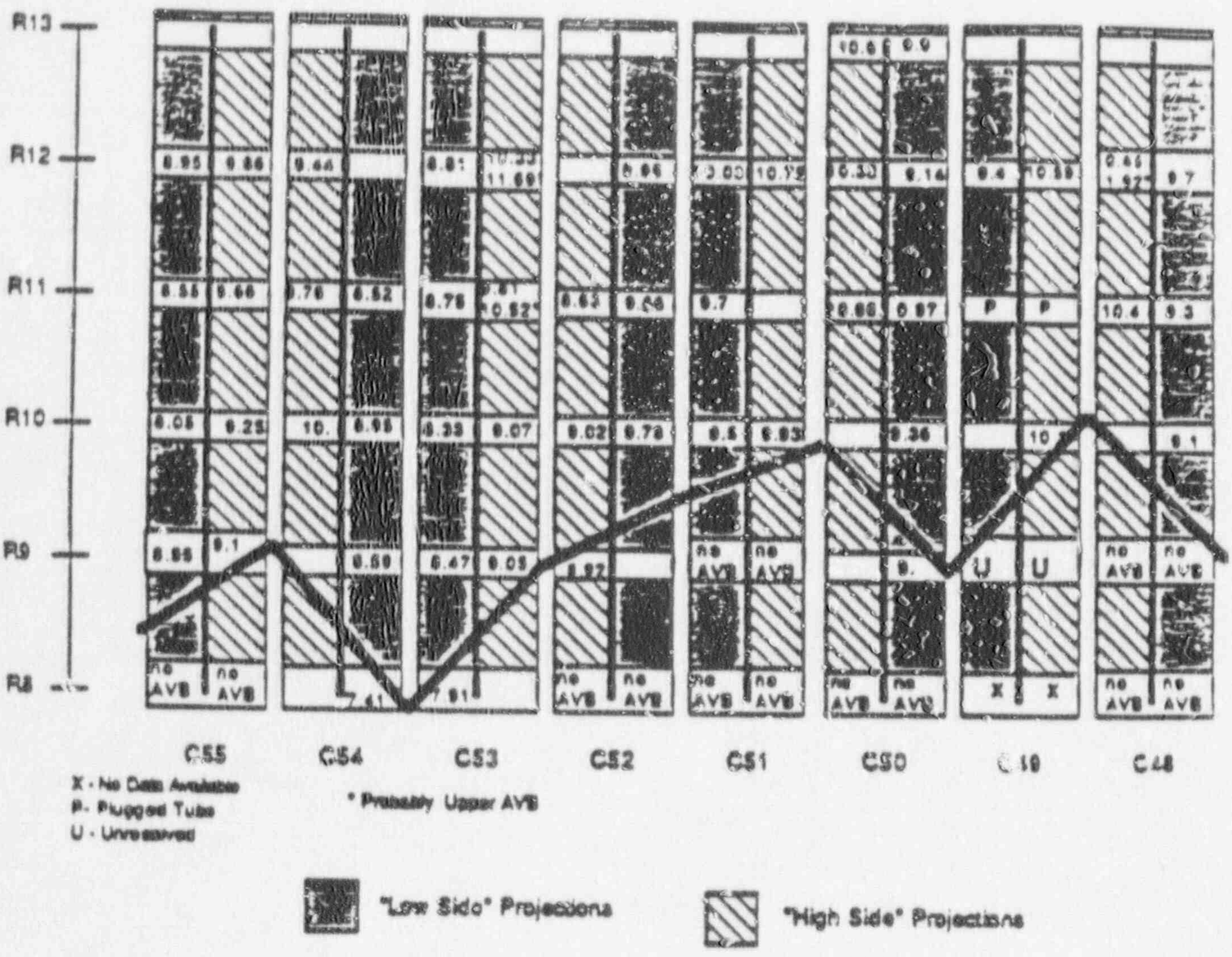

Figure 8-5 North Anna 1, Steam Generator C, R9C51 AVB
[ ]^{a,c} Matrix

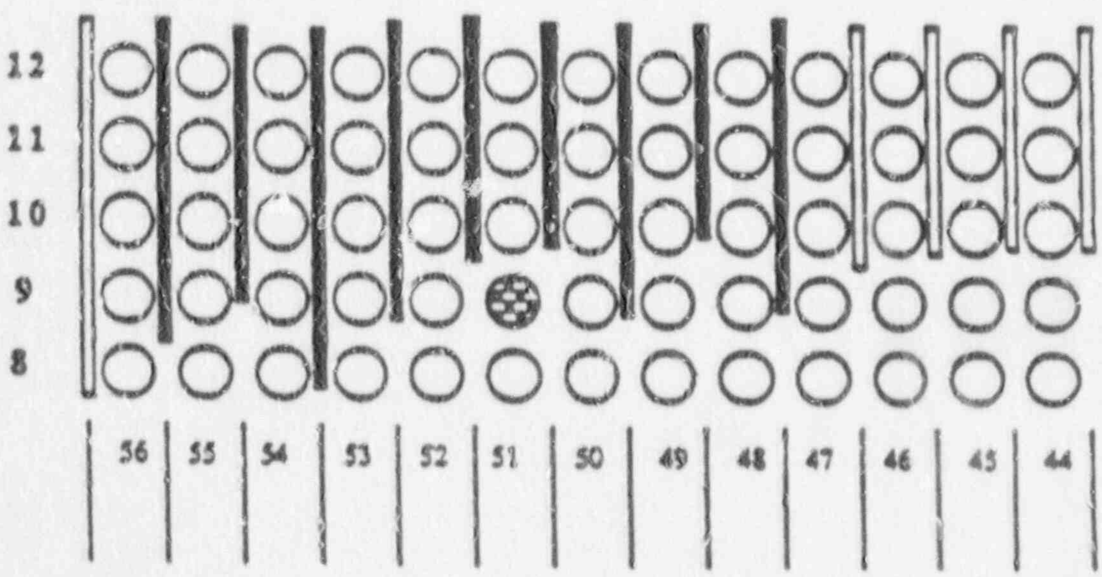

Figure 8-6 North Anna R9C52 Final [ ]^{a,c} Positions
(Configuration 1a)

TYPE OF AVB INSERTION	PEAKING FACTOR	TYPE OF AVB INSERTION	PEAKING FACTOR
	a, c		a, c

Figure 8-7 Final Peaking Factors for V. C. Summer

9.0 STRUCTURAL AND TUBE VIBRATION ASSESSMENTS

9.1 Tube Mean Stress

This section summarizes the analysis to determine stresses in a dented, but undeformed, tube at 100% power. Loads imposed on the tube correspond to steady-state pressure, differential thermal expansion between the tube and the support plate, and a thru-wall thermal gradient. The analysis assumes the tube to be [ ]^{a,c} at cold shutdown.

A summary of the temperature and pressure parameters used for mean stress calculations at 100% power in the vicinity of the top support plate is provided in Table 9-1. The tube temperature corresponds to the average of the primary-side water temperature and the plate temperature. The resulting tube/plate radial interference is [ ]^{a,c}.

Stresses due to differential pressure and interference loads are calculated using finite element analysis with the model shown in Figure 9-1. The model prescribes [

]^{a,c}

Two reference cases were run using the finite element model, the first for a primary-to-secondary side pressure gradient of 1000 psi, and the second for a [ ]^{a,c} inch radial interference between the tube and plate. The pressure case incorporates the axial load on the tube by applying a pressure loading along the top face of the model. Plots showing the stress distributions on the tube outer surface are provided for the two reference cases in Figures 9-2 and 9-3. Thermal bending stresses due to the thru-wall thermal gradient are calculated to be 8.0 ksi using conventional analysis techniques. The combined stress distribution along the tube length, shown in Figure 9-4, was obtained by combining the thermal bending stresses and the reference solutions with appropriate multipliers based on 100% power operating parameters.

The maximum axial tensile stress is 20.3 ksi and occurs approximately 0.133 inch above the top surface of the support plate. Adding, for conservatism, the surface stress due to pressure, 0.94 ksi, gives an applied mean stress of 21.24 ksi. In addition to the applied stress, residual stresses exist in the tube as a result of the manufacturing process. For mill annealed tubes with subsequent straightening and polishing, residual stresses are compressive at the tube surface, but 5-10 mils below the surface, the stress levels change to 10-15 ksi tensile. Combining the applied and residual stresses results in a cumulative mean stress of approximately 36 ksi, assuming tube denting without deformation.

If a tube is dented with deformation, the mean stress is limited by tube yielding. For the case of dented tubes with deformation, the maximum effect of mean stress was incorporated by using $\sigma_{max} = \sigma_y$ in determining stability ratios and fatigue usage.

9.2 Stability Ratio Distribution Based Upon ATHOS

An assessment of the potential for tubes to experience fluidelastic instability in the U-bend region has been performed for each of the tubes in rows eight through thirteen. This analysis utilizes FASTVIB, a Westinghouse proprietary finite element based computer code, and PLOTVIB, a post processor to FASTVIB. These codes predict the individual responses of an entire row of steam generator tubing exposed to a location dependent fluid velocity and density profile. The program calculates tube natural frequencies and mode shapes using a linear finite element model of the tube. The fluid elastic stability ratio U_e/U_c (the ratio of the effective velocity to the critical velocity) and the vibration amplitudes caused by turbulence are calculated for a given velocity/density/void fraction profile and tube support condition. The velocity, density and void fraction distributions are determined using the ATHOS computer code as described in Section 7.3. The WECAN-generated mass and stiffness matrices used to represent the tube are also input to the code. (WECAN is also a Westinghouse computer code.) Additional input to FASTVIB/PLOTVIB consists of tube support conditions, fluidelastic stability constant, turbulence constants, and location dependent flow peaking factors.

This process was performed for the steam generator tubes of a Reference Model D3 and also for the North Anna Row 9 Column 51 tube (R9C51), using similarly appropriate ATHOS models. Ratios of the Reference results to those for North Anna Unit 1 R9C51 provided a quantity that could be used for an initial assessment of the V. C. Summer tubes relative to the ruptured tube at North Anna Unit 1.

These initial relative stability ratios (RSR) were subsequently updated to account for the differences in operating conditions between the Reference Model D3 ATHOS model used in the evaluation and the V. C. Summer conditions. A 1D multiplier was developed and then applied to the RSR corresponding to each tube. A discussion of the 1D ratio methodology has been discussed in Section 7.0. The result of this process is a quantity that describes a specific V. C. Summer tube relative to the ruptured tube at North Anna Unit 1.

Figure 9-5 shows the results of this process for Rows 8 through 12. The relative ratios are obtained using the following conditions for V. C. Summer and North Anna Unit 1:

1) Tube is fixed at the top tube support plate,

2) Void fraction-dependent damping,

3) No AVB supports are active,

4) Location-dependent flow peaking factors.

It is to be noted that the stability ratios plotted in Figure 9-5 are composites of all steam generators using mirror image tubes. That is, any peaking effect for a given tube location indicated on the plot represents the maximum value of the peaking factor in all steam generators at that location.

A horizontal line is drawn at the relative stability ratio value of 0.90. This identifies the point where a ten percent reduction in stability ratio exists relative to North Anna R9C51. (See Section 4.1 for a discussion of the stability ratio reduction criteria.) All the tubes with ratios above this line would be considered to have stability ratios larger than ninety percent of North Anna R9C51.

Figure 9-5 indicates that most tubes in Rows 7 through 11 of the V. C. Summer steam generators are below the 0.9 RSR line. The RSR values for all Row 7 through 13 tubes are below 0.9, with the exception of the following seven tubes:

SG A	SG B	SG C
R9C83	R9C56	R9C29
		R9C106
		R10C23
		R12C5
		R13C5

9.3 Stress Ratio Distribution with Peaking Factor

An evaluation was performed to determine the ratio of the V. C. Summer tube stress over the North Anna R9C51 tube stress. This ratio is determined using relative stability ratios discussed in the previous section, relative flow peaking factors (Table 8-7 factors divided by [ ]^{a,c}), tube size, and bending moment factors. Sections 4.2 and 4.3 contain additional information and describe the calculational procedure used to obtain the results presented in this section. The results presented below are based upon the following conditions:

1) Tube is fixed at the top tube support plate,

2) Damping is void fraction dependent,

3) Tubes have no AVB support,

4) 10% criteria with frequency effects,

5) Location-dependent flow peaking effects

6) Tubes are assumed to be dented with deformation (labeled with denting) or clamped at the top support plate due to crevice corrosion (labeled without denting).

A tube can be considered acceptable if the stress ratio is less than 1.0 when calculated using the procedure described in Sections 4.2 and 4.3, including the conditions listed above, and subject to confirmation of fatigue usage acceptability. Conformance to these requirements implies that the stress acting on a given tube is expected to be insufficient to produce a fatigue event in a manner similar to the rupture that occurred in the R9C51 tube at North Anna Unit 1.

Figure 9-6 shows the results of the stress ratio calculations for each of the V. C. Summer tubes in Rows 7 through 12. Similar to the stability ratios in Figure 9-5, the stress ratios in Figure 9-6 represent the composite ratios for all V. C. Summer steam generators. (Refer to Table 9-2 for salient tubes in individual steam generators). These ratios are applicable for tubes that are dented (tube deformation) at the top tube support plate. This case bounds the clamped tube condition with no tube deformation, i.e., the case corresponding to the NRC definition of denting with top tube support plate corr :on plus magnetite in the crevice without tube deformation. Figur 9-7 contains the results for the case where tube deformation is not present. These figures demonstrate the effects of varying the applied mean stress on the tube. Using the mean stress present in the undented results produces stress ratio values that are lower than stress ratios calculated for tubes in the dented condition.

As can be observed in Figures 9-6, Figure 9-7 and Table 9-2, several tubes have stress ratios that are greater than 1.0. The following tubes have been identified as having stress ratios (both with and without denting) greater than 1.0:

SG A	SG B	SG C
R9C83	R9C56	R9C29
		R9C106
		R10C23
		R12C5
		R13C5

As noted in Section 9.5, it is recommended that all tubes with stress ratios exceeding 1.0 and that have cumulative usage greater than 1.0 (such as the tubes listed above) be removed from service.

To assist SCE&G in evaluating operational issues associated with the installation of cable dampers, the lowest added damping value determined from the available tests was assumed to be provided by cable dampers in the seven tubes of interest for V. C. Summer. With this assumed minimum added damping value of [ ],^{a,c} all of the stress ratios in the seven tubes of interest are below [

],^{a,c} R12C5 would have a stress ratio of

[

]^{a,c} or less. With this assumption, tubes that had not initiated a crack would be predicted to be acceptable for continued operation with a cable damper installed.

An evaluation has also been performed to determine the required relative flow peaking that will produce a stress ratio not greater than 1.0. Figure 9-8 contains the results of this process for all tubes in Rows 7 through 12. The figure was generated using the conditions outlined previously with the additional constraint that the tubes are dented. Note that this figure reads opposite of the previous figures, i.e., the top curve in the figure corresponds to Row 7 and the bottom curve corresponds to Row 12. Maximum Allowable Relative Flow Peaking is the required relative flow peaking (0.68 corresponds to no flow peaking) which, if used on the given tube, will produce a stress ratio (with denting) not to exceed 1.0. This curve can be used to identify the relative flow peaking required before preventive action would be recommended and, when used in conjunction with the actual flow peaking associated with each tube, to determine the margin (if any) present. This has also been performed in Table 9-2. The column with heading "Max Allow Rel FPEAK" identifies the relative flow peaking factor that would be permitted, on a tube by tube basis, before the stress ratio criteria would be exceeded. As can be observed in the table and figure, the inner row tubes have larger values of allowable relative flow peaking when compared to the outer rows.

9.4 Cumulative Fatigue Usage

All unsupported tubes having stress ratios $\leq$ 1.0 will have a maximum stress amplitude that is < 4.0 ksi (from 9.5 ksi), since a 10% reduction in the stability ratio for the North Anna Row 9 Column 51 tube was the criteria basis. The stability ratios for the V. C. Summer tubing are based on the Cycle 5 operating parameters and assume future operation with the same parameters. The tubes are not expected to rupture as a result of fatigue if 1) they meet the stress ratio criteria of $\leq$1.0 and 2) their current and future fatigue usage will total less than 1.0.

Based on the above analyses, most V. C. Summer tubes meet the relative stress ratio criteria. Seven tubes do not meet the stress ratio criteria. Table 9-2 provides a summary of the combined relative stability ratios and the stress ratios for salient unsupported tubes in Rows 7 through 13.

Of the seven tubes mentioned above, SG-A R9C83, SG-B R9C56, SG-C R12C5 and SG-C R13C5, if previously dented or if becoming dented at the beginning of an operating cycle with current operating conditions, could potentially have tube fatigue usage factors exceeding 1.0 within the cycle, and therefore require preventive action. Note that with the exception of SG-B R9C56, which was evaluated as having magnetite packing at one of the two top tube support plate intersections, all of these four times were evaluated from the October 1988 outage inspection data as "clean" at the top tube support plate intersections. Two additional tubes, SG-C R9C29 (magnetite in one top TSP and clean in the other) and SG-C R10C23 (magnetite in both top TSP crevices), potentially have current accumulated fatigue usages as high as 1.0, if it is conservatively assumed that denting began at the start of the first fuel cycle, and also therefore require preventive action. SG-C R9C106 was evaluated as having no denting at the top tube support plate elevation based upon examination of the October 1988 inspection data, but may have accumulated as much as 0.34 fatigue usage if it became dented or magnetite-packed at the beginning of Cycle 5. If dented and operating at Cycle 5 conditions, it will continue to accumulate fatigue usage at the rate of 0.34 per year, and is also recommended for preventive action.

Acceptability of the V. C. Summer tubing for fatigue is accomplished by demonstrating the acceptability of the tube remaining in service with the highest stress ratio that does not exceed the 1.0 stress ratio criteria. For V. C. Summer this tube is SG-A R9C55 and has a stress ratio of [ ]^{a,c} for Cycle 5 operating conditions. Assuming this worst case tube (R9C55) has been dented since the first cycle and continues to operate with steam pressures at or above 941 psia, the total usage including the remaining term of the operating license would be 0.36.

9.5 Effect of Steam Pressure on Potentially Susceptible Tubes

An additional fatigue evaluation of the V. C. Summer tubing was performed to examine the effect of reduced steam pressure and coastdown power levels, with the objective of demonstrating the acceptability of the tube remaining in service with the highest stress ratio that does not exceed the 1.0 stress ratio criterion. Parametric analysis was performed to determine the relative stability ratio (RSR) multipliers and stress ratios for full power steam pressures below the reference steam pressure (941 psia) and it was determined that the limiting tube, SG-A R9C55, does not exceed the 1.0 stress ratio criterion for steam pressures above 905 psia. Since SCE&G is considering power coastdown operation, the RSR multipliers were also evaluated assuming a constant volumetric steam flow for pressures below 905 psia. (The 905 psia steam pressure is a lower bound, full power steam pressure value; V. C. Summer turbine tests indicate the "best estimate" value of the Valves Wide Open (VWO) steam pressure to be 915 psia). For the reduced power levels associated with operation below the assumed 905 psia VWO limit, the RSR multipliers decrease, and the fatigue results remain bounded. Therefore, assuming that the worst case tube (SG-A R9C55) has been dented since the first cycle and the turbine Valves Wide Open limit is not reduced below 905 psia, all tubes remaining in service at V. C. Summer are acceptable for operation through the end of the current operating license with power levels at or below the 2785 MWt.

9.6 Conclusions

Seven tubes were recommended for preventive action: SG-A R9C83, SG-B R9C56, SG-C R12C5, SG-C R13C5, SG-C R10C23, SG-C R9C29, and SG-C R9C106. These tubes were removed from service in April 1990 with the installation of cable dampers, hot leg plugs, and cold leg sentinel plugs. The tubes remaining in service in the V. C. Summer steam generators are not expected to be susceptible to high-cycle fatigue rupture at the top tube support plate in a manner similar to the rupture which occurred at North Anna #1, assuming that the turbine Valves Wide Open limit is not reduced below 905 psia, through the end of the current operating license with power levels at or below 2785 MWt.

Reference:

9-1 Westinghouse Research & Development Report 77-1D2-TUCOR-R2, "Residual Stresses in Inconel 600 Steam Generator Tubes - Part II: Straight Tubes", Westinghouse Research Laboratories, Proprietary Class 2, D. L. Harrod, October 21, 1977.

Table 9-1

100% Power Operating Parameters
V. C. Summer
Bounding Values for Mean Stress Calculations

Primary Pressure	=	2250 psia
Secondary Pressure	=	941 psia
Pressure Gradient	=	1309 psi

Primary Side Temperature *	=	587°F
Secondary Side Temperature	=	537°F
Tube Temperature	=	562°F

* Average of T_{hot} = 618°F and T_{cold} = 556°F.

TABLE 9-2

V. C. Summer Tubes With Significant RSRs or Stress Ratios

Steam Gen.	Row No.	Col. No.	Flow Peaking	Max Allow Rel. FPEAK		RSR* FPEAK	Stress Ratio W/Dent	Stress Ratio W/O Dent
A	8	11			a,c	0.549	0.10	0.10
		22				0.524	0.08	0.08
	9	55				0.818	0.76	0.70
		63				0.801	0.68	0.62
		70 & 71				0.725	0.39	0.36
		83				1.155	>2.00	>2.00
B	7	11				0.546	0.12	0.11
	8	66				0.672	0.31	0.29
		74				0.607	0.18	0.16
	9	56				1.168	>2.00	>2.00
		110				0.737	0.43	0.39
C	7	88				0.544	0.12	0.11
	8	93				0.555	0.11	0.10
		97 & 98				0.595	0.16	0.14
	9	11 & 12				0.710	0.35	0.32
		23				0.636	0.19	0.17
		29				0.946	1.78	1.63
		106				0.937	1.63	1.49
	10	2-8				0.740	0.37	0.34
		11 & 12				0.738	0.36	0.33
		23				0.968	1.88	1.73
		106				0.738	0.36	0.33
		113				0.545	0.07	0.06
	11	4-8				0.856	0.70	0.64
	12	5				1.403	>2.00	>2.00
	13	5				1.751	>2.00	>2.00

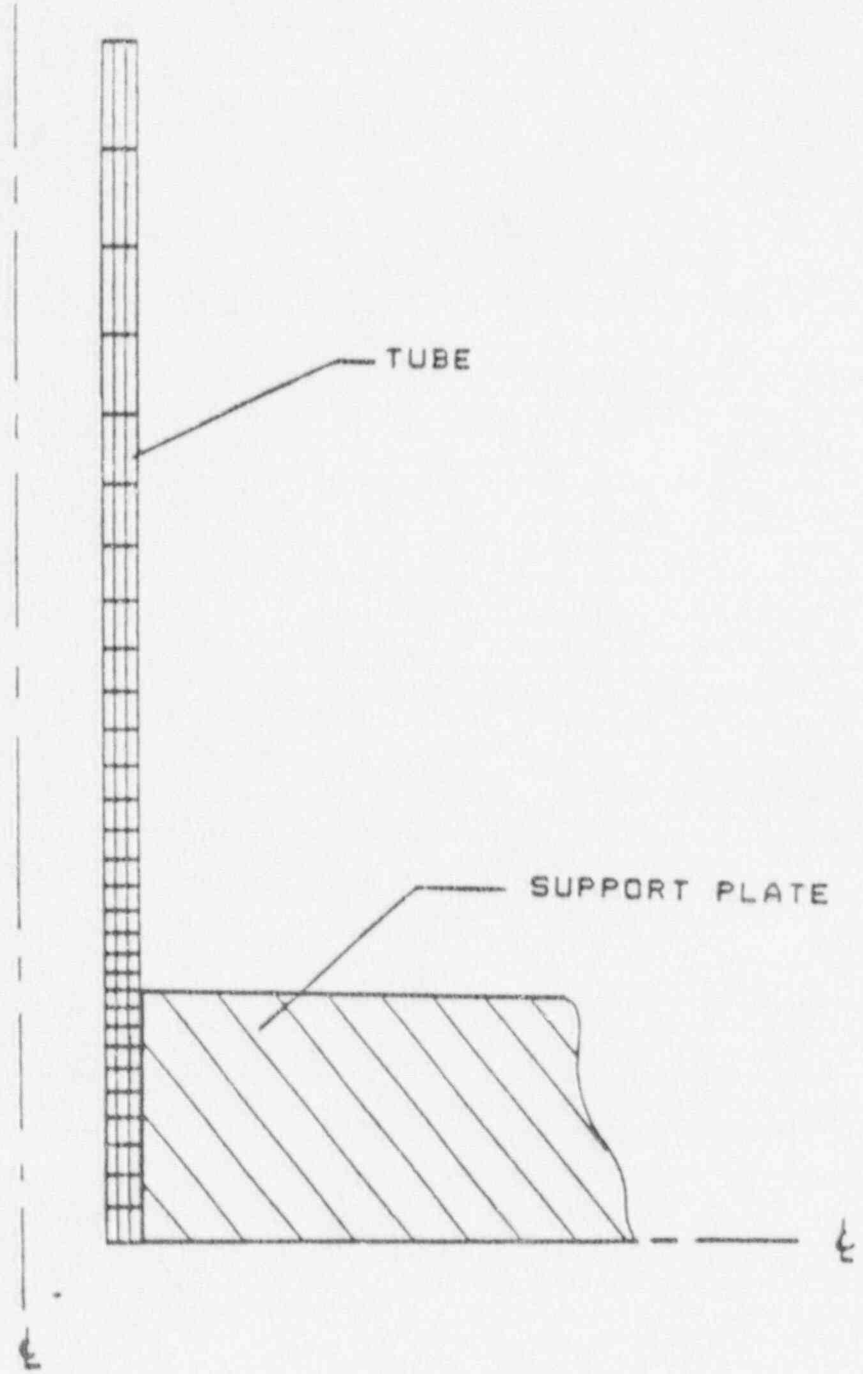

Figure 9-1 Axisymmetric Tube Finite Element Model

a,c

Figure 9-2 Dented Tube Stress Distributions
Pressure Load on Tube

a,c

Figure 9-3 Dented Tube Stress Distributions
Interference Load on Tube

a,c

Figure 9-4

Dented Tube Stress Distributions

Combined Stress Results for V. C. Summer

a,c

Figure 9-5

Relative Stability Ratios Using MEVF Dependent Damping

V. C. Summer - (Composite of All Steam Generators with Umbrella Flow Peaking)

a,c

Figure 9-6

Stress Ratio vs. Column Number - Dented Condition - V. C. Summer
(Composite of All Steam Generators with Umbrella Flow Peaking)

a,c

Figure 9-7

Stress Ratio vs. Column Number - Undented Condition - V. C. Summer
(Composite of All Steam Generators with Umbrella Flow Peaking)

a,c

Figure 9-8

Maximum Allowable Relative Flow Peaking - V. C. Summer